Journal of Materials Chemistry A

ROYAL SOCIETY OF CHEMISTRY

PAPER

View Article Online
View Journal



Cite this: DOI: 10.1039/d6ta02200f

# Hybrid carbonate and redox systems for thermochemical energy storage

Mónica Salazar-Lago,†[a] Ana Castro-Chincho,[a] Pedro E. Sánchez-Jiménez,*[a] Luis A. Pérez-Maqueda*[a] and Antonio Perejón *[ab]

A hybrid thermochemical energy storage material based on the coupling of carbonate ($CaCO_3$/CaO) and redox (CuO/$Cu_2O$) reactions is herein proposed. This integrated $CaCO_3$/CuO system enables the simultaneous contribution of calcium looping and redox processes within a single multifunctional composite. The resulting materials exhibit synergistic enhancements in reactivity, solar absorptance, and thermal conductivity arising from phase interactions between carbonate and oxide domains. Simultaneous operation of both reaction schemes was achieved under atmosphere-switching and fixed-atmosphere conditions, although the extent of conversion varied depending on the reaction conditions. The influence of CuO content and preparation method on multicycle performance was systematically evaluated. A composite containing a 50 : 50 $CaCO_3$/CuO mass ratio prepared by wet ball milling delivered the most balanced performance over repeated charge/discharge cycles. Conversion and energy storage density analyses demonstrate that both components actively contribute to the total stored energy, with their relative contributions depending on the operating conditions. Beyond providing an additional redox-based energy contribution, CuO mitigates sintering in the $CaCO_3$/CaO system, thereby enhancing cycling stability. Optical and thermal characterization further revealed a marked improvement in solar absorptance and thermal conductivity compared with $CaCO_3$ alone. These finding establish $CaCO_3$/CuO composites as a new material design platform for integrated thermochemical energy storage.

Received 13th March 2026
Accepted 6th May 2026

DOI: 10.1039/d6ta02200f

rsc.li/materials-a



## 1. Introduction

Concentrated Solar Power (CSP) stands as a promising renewable energy technology; however, dispatchability issues arising from the intermittency and variability of solar radiation limit its deployment. Typically, solar irradiance peaks around midday, while the highest energy demand occurs approximately one hour after sunset.[1] This temporal mismatch between energy availability and demand highlights the need for advanced storage technologies capable of bridging this gap.

Currently, state-of-the-art CSP plants rely on sensible heat storage (SHS) systems to store solar energy.[2] These systems employ molten salts, which are heated to store energy and cooled to release it. Despite their widespread use, molten salts present several drawbacks, including corrosiveness, which can damage heat exchangers, piping and storage tanks. Additionally, their operational temperature is relatively low (around 600 °C), as they decompose at higher temperatures. Moreover, their relatively high melting point (200 °C) necessitates auxiliary systems to prevent solidification and consequent pipeline blockages.[3,4]

Thermochemical energy storage (TCES) represents an attractive alternative, as it is based on reversible reactions that offer high energy density, negligible heat losses over long storage periods, and operation at elevated temperatures, thereby enabling high electrical efficiencies.[5] Materials for TCES must combine excellent reversibility with high reaction enthalpies,[6–8] while also being economically viable, requiring abundance and low cost.[9,10] Several candidate systems are currently under investigation, including hydrides, hydroxides, redox couples, and carbonates.[11,12] Eqn (1) illustrates a generic reversible endothermic reaction, in which reactant A is converted into products B and C upon the input of heat:

$$A + \Delta H \rightleftharpoons B + C \quad (1)$$

In the TCES–CSP framework, heat input is provided by solar radiation, either directly or indirectly. Direct absorption receivers transfer solar radiation directly to the reactive

[a]Instituto de Ciencia de Materiales de Sevilla (C.S.I.C.-Universidad de Sevilla), C. Américo Vespucio 49, Sevilla, 41092, Spain. E-mail: aperejon@us.es; maqueda@icmse.csic.es; pedro.enrique@icmse.csic.es

[b]Departamento de Química Inorgánica, Facultad de Química, Universidad de Sevilla, 41012 Sevilla, Spain

† Present address: Thermal Spray Group, Industry and Transport Division, TECNALIA, C/Gabiria 82-84, 20305 Irun, Spain; Departamento de Química Aplicada, Facultad de Química, Universidad del País Vasco/Euskal Herriko Unibertsitatea (UPV/EHU), 20018 Donostia-San Sebastián, Spain.

material, avoiding intermediate surfaces and allowing operation at higher temperatures.[13,14] In this case, the efficiency of radiative heat transfer depends strongly on the absorption capacity of the material.[15] In contrast, indirect receivers rely on a primary absorber to transfer heat to the reactive medium, which generally leads to higher heat losses.[16]

In a typical cycle, the reactant decomposes into products that are stored separately. When energy is required, these products are fed into a reactor where the exothermic reverse reaction takes place, releasing the stored heat, which can then be converted into electricity *via* turbines.[8,9,17]

Calcium Looping (CaL) is a technology based on the reversible calcination and carbonation reaction of the $CaCO_3$/CaO system:

$$CaCO_3\,(s) \rightleftharpoons CaO\,(s) + CO_2\,(g), \quad \Delta H = \pm 3178.6\ \text{kJ kg}^{-1}\ \text{CaO} \tag{2}$$

Originally proposed for $CO_2$ capture, it has also been identified as a promising alternative to molten salts for energy storage in CSP plants (CaL-CSP). Compared with molten salts, CaL provides higher energy density and the ability to operate at higher temperatures.[11,12,18]

The concept of utilizing carbonates relies on the endothermic nature of decarbonation (calcination), in which energy is consumed to decompose $CaCO_3$ into CaO and $CO_2$. This reaction can be carried out in an inert gas (*e.g.*, He and $N_2$) or under low $CO_2$ partial pressures, which reduces the required temperature.[12,19] The reverse carbonation reaction, responsible for energy release, occurs within the range of 650–900 °C, making CaL highly compatible with efficient power cycles.[20,21] Recently, the CaO carbonation technology has been successfully tested at the kW-scale in a novel entrained flow reactor, constructed within the framework of the SOCRATCES EU project, showing its potential for deployment in MW-scale solar plants.[22]

Despite its high theoretical energy storage density, the $CaCO_3$/CaO system presents several limitations that hinder its practical application, including sintering-induced deactivation during cycling, low solar absorptance, and limited thermal conductivity.[23–25] These drawbacks restrict both the efficiency and the stability of the process under realistic operating conditions. Strategies employed to address these issues include the use of additives, morphological control through tailored preparation methods, and optimized cycling conditions, all while minimizing cost, which remains a critical barrier to large-scale deployment.[26–30] In addition, additives are often introduced to enhance optical properties, which is particularly relevant for direct absorption receivers,[31] and thermal properties.[32,33]

In this work, composites of calcium carbonate and copper oxide are investigated as candidate materials for TCES.

Copper oxide belongs to a widely studied TCES approach that involves the use of metal oxide redox couples.[34,35] In these systems, the endothermic reduction step consumes energy to partially reduce the oxide, releasing oxygen and lowering the oxidation state of the metal. This scheme offers the additional advantage of employing air or other gases as both heat transfer fluids and reactants.[36,37] The choice of suitable redox couples for CSP applications depends on several criteria, including reaction temperature, reversibility, toxicity, and cost. Many potential candidates have been discarded due to insufficient performance at either low or high temperatures,[38] or because of unfavorable economic or environmental characteristics.[8] Taking these limitations into account, among the most promising systems are $BaO_2$/BaO, CuO/$Cu_2O$, $Co_3O_4$/CoO, and $Mn_2O_3$/$Mn_3O_4$, which exhibit reaction temperatures in air between 900 and 1300 °C.[39–47] Recent studies have validated a kW-scale redox reactor/heat exchanger that operates continuously while transferring heat to an independent high-temperature heat transfer fluid.[48]

The CuO/$Cu_2O$ redox pair follows eqn (3):

$$2CuO(s) \rightleftharpoons Cu_2O(s) + \frac{1}{2}O_2(g) \quad \Delta H = \pm 1083.3\ \text{kJ per kg}\ Cu_2O \tag{3}$$

In this context, the combination of two active materials creates a synergistic effect, as one component stabilizes the other by mitigating the loss of reactivity over cycling. Furthermore, unlike inert stabilizers used in other studies, both $CaCO_3$ and CuO contribute to the overall energy balance. Finally, optical and thermal properties are significantly enhanced, making the composites well suited for direct irradiation applications. The experimental conditions were optimized to allow the simultaneous occurrence of $CaCO_3$ calcination/carbonation and CuO reduction/oxidation. While CaO–CuO composites have previously been investigated for $CO_2$ capture, where CaO regeneration is driven by the exothermic reduction of CuO with methane, this hybrid system has not yet been explored for thermochemical energy storage.[49–51]

## 2. Materials and methods

### 2.1. Materials

The materials used in this study were calcium carbonate ($CaCO_3$, by KSL Staubtechnik GmbH, Germany; average particle size 80 μm), and copper(II) oxide (CuO, IOLITEC nanomaterials, 99.9%, 40–80 nm).

### 2.2. Sample preparation

The composites were prepared using three different mixing procedures, two of which involved mechanical treatments and a third based on freeze granulation followed by lyophilization. The selected preparation methods were chosen to provide different levels or mixing and microstructural control. Dry ball milling was used as a simple and reproducible baseline, while wet ball milling was expected to improve particle dispersion and interfacial contact between both components of the composites. Freeze granulation was employed as an advanced technique to promote a more homogeneous microstructure and controlled particle assembly, potentially enhancing the stability during cycling.

Dry ball milling was performed in an Emax mill (Retsch) using stainless steel jars with a volume of 125 ml, containing

 

100 stainless steel balls (6 mm in diameter) and 3 g of sample. Milling consisted of two cycles of 2 min each at 500 rpm. This mixing method was first explored to investigate the effect of the relative amounts of $CaCO_3$ and CuO on reactivity toward carbonation and oxidation. Three samples were prepared with different $CaCO_3$/CuO mass ratios. This approach enabled a systematic evaluation of the influence of composition using a simple and reproducible method, allowing the identification of the most promising $CaCO_3$/CuO ratio.

Wet ball milling and freeze granulation were subsequently investigated for a 50 : 50 mass ratio of $CaCO_3$ and CuO, which was identified as the most promising formulation based on the preliminary screening. This strategy allowed the more complex preparation methods to focus on the compositions of greatest interest. Wet ball milling was carried out in an Orto-Alresa ball mill. 4 g of $CaCO_3$ and 4 g of CuO were placed into a 500 ml plastic container along with 50 alumina balls (10 mm in diameter). Then, 100 ml of distilled water was added, and the sample was milled for 3 h. Afterwards, the slurry was transferred to a 250 ml beaker and dried in an oven at 90 °C until complete solvent evaporation. For the freeze granulation process, 5 g of $CaCO_3$ and 5 g of CuO were dispersed in Milli-Q water under stirring at room temperature to ensure adequate homogenization. An ultrasonic bath was then applied to deagglomerate the particles. The suspension was transferred into a 20 ml syringe and pumped through a fine nozzle, producing small droplets that were collected in liquid nitrogen to achieve instantaneous freezing. The frozen granules were subsequently freeze-dried (LYOQUEST-55 plus, Telstar) for 24 h, with the condenser temperature set to −60 °C. Table 1 summarizes the sample codes, preparation methods, and relative amounts of $CaCO_3$ and CuO, while Fig. 1 outlines the different methods employed to prepare the samples.

### 2.3. Thermogravimetric analysis

The multicycle performance of the samples was evaluated by thermogravimetry using a simultaneous thermal analyzer STA 449 F5 Jupiter (Netzsch). This instrument features a vertically arranged SiC furnace, allowing sample loading from the top, and provides measurements from room temperature up to 1600 °C, with heating and cooling ramps ranging from 0.001 to 50 °C $min^{-1}$ and a microbalance resolution of 0.1 μg.

Table 1 Summary of sample codes, preparation methods, and relative mass ratios ($f$) of $CaCO_3$ and CuO. Abbreviations: D = dry ball milling; W = wet ball milling; F = freeze granulation

| Sample name | Preparation method | $f_{CaCO_3}$ (% mass) | $f_{CuO}$ (% mass) |
|---|---|---|---|
| DCa95Cu05 | D | 95 | 5 |
| DCa80Cu20 | D | 80 | 20 |
| DCa50Cu50 | D | 50 | 50 |
| WCa50Cu50 | W | 50 | 50 |
| FCa50Cu50 | F | 50 | 50 |

The tests consisted of repeated cycles in which endothermic (charge) and exothermic (discharge) reactions were studied. During the endothermic reactions, $CaCO_3$ and CuO were calcined and reduced, respectively. In the exothermic reactions, the products of the endothermic steps, CaO and $Cu_2O$, underwent carbonation and oxidation, respectively.

The selection of the gas compositions was guided by the thermodynamic equilibrium of the CuO/$Cu_2O$ system,[43,52] with the objective of aligning the reduction and oxidation of CuO with the operating windows required for the calcium looping process.[12,28] By tuning the oxygen partial pressure and temperature, the CuO/$Cu_2O$ redox transition was designed to occur under conditions compatible with $CaCO_3$ calcination and CaO carbonation. Thus, two different sets of experimental conditions were explored to investigate the reactivity of the $CaCO_3$/CuO system. In the first set, the temperature was held constant at 850 °C throughout the cycle. Calcination of $CaCO_3$ and reduction of CuO were performed under a pure nitrogen atmosphere. Carbonation and oxidation were carried out under a $CO_2$ atmosphere containing 3% $O_2$ by volume (due to instrumental limitations, a small amount of protective gas, 4% $N_2$ by volume, was required). These conditions are referred to as charge–$N_2$/discharge–$CO_2$–$O_2$. In the second set, a closed-loop process was employed using an atmosphere composed of 93% $CO_2$, 3% $O_2$, and 4% $N_2$ by volume for both steps. In this case, calcination and reduction were performed at 950 °C, while carbonation and oxidation were conducted at 800 °C. These conditions are referred to as charge/discharge–$CO_2$–$O_2$.

The selected temperatures were not intended to optimize each individual reaction independently, but rather to ensure thermodynamic compatibility between the $CaCO_3$/CaO and CuO/$Cu_2O$ systems under process-relevant conditions.

Table 2 summarizes the experimental conditions used in this work. The multicycle performance of each sample was assessed over 20 calcination–reduction and carbonation–oxidation cycles under both conditions. Heating and cooling rates of 20 °C $min^{-1}$ were applied, and each isothermal stage was maintained for 20 minutes. All experiments were repeated at least twice using independently prepared samples, showing high reproducibility with deviations within ±2%, which was further confirmed by additional repetitions in selected cases.

Fig. 2 illustrates the thermodynamic equilibrium diagrams of the $CaCO_3$/CaO (Fig. 2a) and CuO/$Cu_2O$ systems (Fig. 2b), with the temperature and gas compositions used in both experimental schemes superimposed. In the $CaCO_3$/CaO diagram, the selected charge and discharge conditions fall on opposite sides of the equilibrium boundary, ensuring reversible calcination and carbonation. Similarly, the CuO/$Cu_2O$ diagram shows that the imposed oxygen partial pressures and temperatures place the system within the stability domains of CuO and $Cu_2O$ during oxidation and reduction, respectively. This confirms that both reaction pairs are thermodynamically compatible with the chosen operating windows, enabling their coupled operation within the same thermochemical cycle.

The two operating modes represent complementary scenarios relevant for practical thermochemical energy storage. The first configuration (charge–$N_2$/discharge–$CO_2$–$O_2$) provides

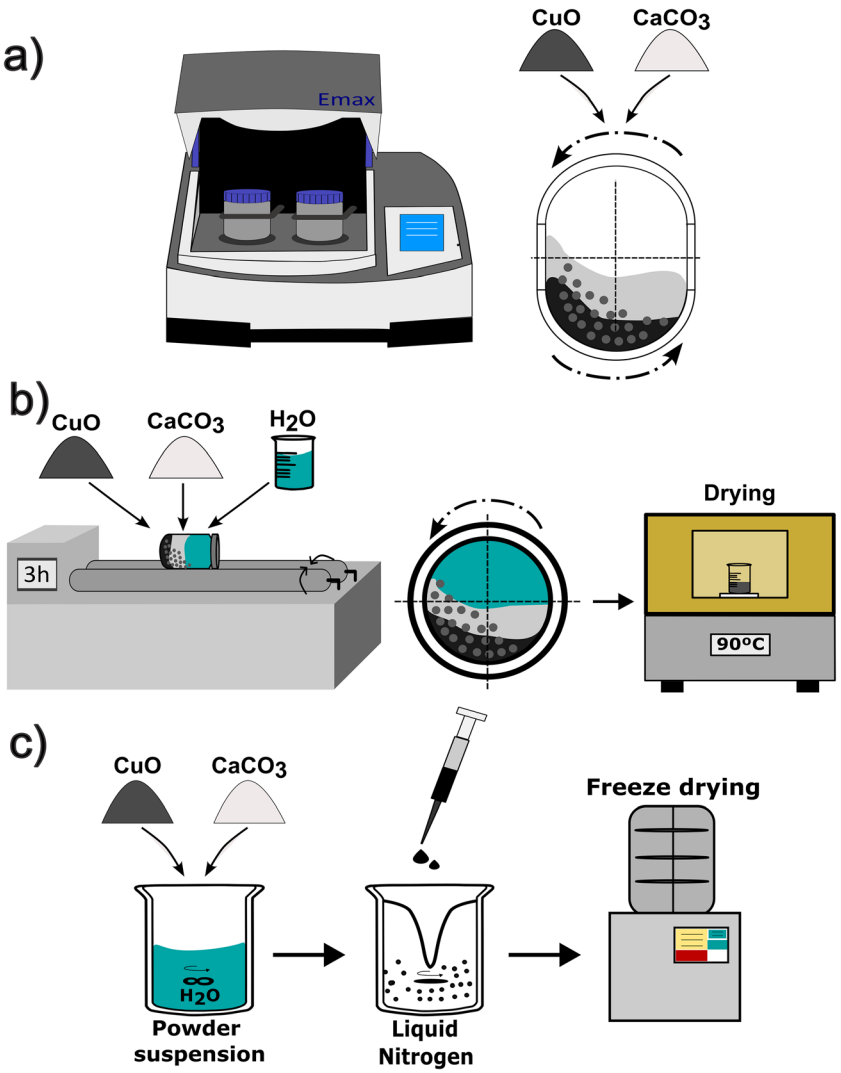


Fig. 1 Schematic representation of the procedures used to prepare $CaCO_3$/CuO composites: (a) dry ball milling, (b) wet ball milling, and (c) freeze granulation followed by lyophilization.

a controlled environment that decouples calcination–reduction from carbonation–oxidation, allowing the intrinsic reactivity of the hybrid $CaCO_3$/CuO system to be assessed under moderate conditions. The second configuration (charge/discharge–$CO_2$–$O_2$) simulates a more realistic closed-loop process, in which a single reactive gas mixture is used and temperature swings are required to drive the reactions.

### 2.4. Determination of the conversions

The overall reactive performance of the $CaCO_3$/CuO hybrid system was evaluated in terms of the total conversion, based on the net mass gain during the discharge step, arising from the carbonation and oxidation reactions. Thus, the total conversion at each $N$ cycle, $X_{T,N}$, was calculated as the ratio between the experimentally measured % mass gain and the maximum

Table 2 Experimental conditions for multicycle performance tests of $CaCO_3$/CuO

| Test | Charge–$N_2$/Discharge–$CO_2$–$O_2$ | | Charge/Discharge–$CO_2$–$O_2$ | |
|---|---|---|---|---|
| | Calcination / Reduction | Carbonation / Oxidation | Calcination / Reduction | Carbonation / Oxidation |
| *Temperature* (°C) | 850 | | 950 | 800 |
| *Atmosphere* | 100% $N_2$ | 93% $CO_2$ + 3% $O_2$ + 4% $N_2$ | 93% $CO_2$ + 3% $O_2$ + 4% $N_2$ | |

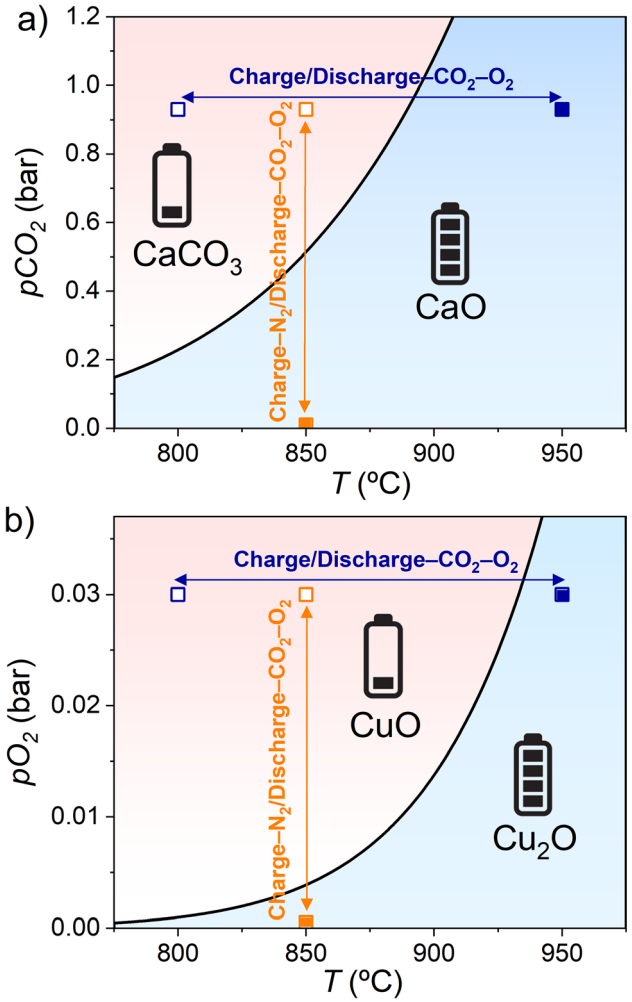


Fig. 2 Thermodynamic equilibrium diagrams of the (a) $CaCO_3$/CaO and (b) CuO/$Cu_2O$ systems, showing the experimental temperature and gas composition conditions used under the charge–$N_2$/discharge–$CO_2$–$O_2$ and charge/discharge–$CO_2$–$O_2$ operating modes. Markers indicate the charge and discharge conditions relative to the phase stability boundaries.

theoretical % mass gain expected if CaO and $Cu_2O$ underwent complete carbonation and oxidation respectively, accounting for their respective mass fractions in the composite:

$$X_{T,N} = \frac{m_{T,N}}{m_{theo,T}} \quad (4)$$

where $m_{T,N}$ is the experimental % mass increase of the sample, and $m_{theo,T}$ is the maximum theoretical % mass gain, calculated as:

$$m_{theo,T} = f_{CaCO_3}\left(\frac{W_{CO_2}}{W_{CaCO_3}}\right) + f_{CuO}\left(\frac{W_{O_2}}{4W_{CuO}}\right) \quad (5)$$

where $f_{CaCO_3}$ and $f_{CuO}$ are the mass percentages of $CaCO_3$ and CuO in the composite, respectively (Table 1). The parameters $W_{CO_2}$, $W_{CaCO_3}$, $W_{O_2}$, and $W_{CuO}$ are the corresponding molar masses.

The CaO conversion at each $N$ cycle was calculated from the % mass gain attributable to carbonation during the discharge step ($m_{CO_2,N}$), normalized to the maximum theoretical % mass increase corresponding to complete carbonation ($m_{theo,CO_2}$):

$$X_{CaO,N} = \frac{m_{CO_2,N}}{m_{theo,CO_2}} = \frac{m_{CO_2,N}}{f_{CaCO_3}\left(\frac{W_{CO_2}}{W_{CaCO_3}}\right)} \quad (6)$$

Similarly, $Cu_2O$ conversion at each $N$ cycle was obtained from the experimental % mass gain due to oxidation ($m_{O_2,N}$), normalized to the maximum theoretical % mass increase corresponding to full oxidation ($m_{theo,O_2}$):

$$X_{Cu_2O,N} = \frac{m_{O_2,N}}{m_{theo,O_2}} = \frac{m_{O_2,N}}{f_{CuO}\left(\frac{W_{O_2}}{4W_{CuO}}\right)} \quad (7)$$

It should be noted that the conversion values correspond to reacted mole fractions, as they are determined from the mass gain associated with $CO_2$ and $O_2$ uptake and normalized to the corresponding theoretical molar amounts dictated by the stoichiometry of the reactions.

### 2.5. Energy storage densities

The gravimetric energy densities ($D_m$) for the carbonation and oxidation processes (discharge) were determined separately for each $N$ cycle. For the calcined and reduced materials, they are defined as:

$$D_{m,CaO,N} = X_{CaO,N} \times \Delta H_{carb} \quad (8)$$

$$D_{m,Cu_2O,N} = X_{Cu_2O,N} \times \Delta H_{ox} \quad (9)$$

where $\Delta H_{carb}$ and $\Delta H_{ox}$ are the enthalpies of carbonation (eqn (2), 3178.57 kJ $kg^{-1}$ CaO) and oxidation (eqn (3), 1083.3 kJ $kg^{-1}$ $Cu_2O$), respectively.

The total gravimetric energy density ($D_{m,T,N}$) for each cycle is defined as the sum of the individual contributions:

$$D_{m,T,N} = D_{m,CaO,N} + D_{m,Cu_2O,N} \quad (10)$$

The maximum theoretical gravimetric energy densities for CaO and $Cu_2O$ are 3.179 MJ $kg^{-1}$ and 0.902 MJ $kg^{-1}$, respectively. The energy storage densities accumulated over the 20 cycles was calculated by integrating the cycle-resolved energy densities.

### 2.6. Sample characterization

The crystal structure of the samples, both before and after cycling, was investigated by X-ray diffraction (XRD) using a Miniflex 600 diffractometer (Rigaku). The instrument employs Cu-K$\alpha$ radiation and operates at 15 mA and 40 kV. Data were collected over a $2\theta$ range of 20°–70°. Microstructural analyses were performed using Scanning Electron Microscopy (SEM, HITACHI S4800). Elemental composition of the sample surfaces was determined by energy-dispersive X-ray spectroscopy (EDX).

The optical properties of the composites were evaluated at room temperature by UV-Vis-NIR spectroscopy in the 300–

2000 nm range using a Cary 5000 spectrophotometer (Agilent Technologies). Diffuse reflectance measurements were carried out using powdered samples placed in a sample holder and analyzed with an integrating sphere to ensure accurate collection of scattered radiation. The absorptance was calculated from the reflectance data assuming negligible transmittance.

Thermal conductivity of the samples was measured by laser flash analysis (LFA 1000, Linseis) under airflow at 400 °C, a temperature selected to avoid the decomposition of $CaCO_3$ and thus preserve the original phase composition during the experiment. The thermal conductivity was calculated from the measured thermal diffusivity, specific heat capacity, and sample density. The specific heat capacity was determined by differential scanning calorimetry (DSC Q20, TA Instruments). Disc-shaped samples were used for the measurements. It should be noted that, under actual operating conditions, the composition and microstructure of the materials evolve due to cyclic calcination–carbonation and redox reactions. Therefore, the reported values correspond to the initial (uncycled) state and are intended to provide a comparative assessment between the precursors and the as-prepared composites.

# 3. Results and discussion

## 3.1. Thermogravimetric analysis under test conditions

Fig. 3 shows the time evolution of the mass percentages (red lines) of unmixed $CaCO_3$ and CuO, for a representative cycle under the two test conditions employed in this work. The corresponding temperature programs are also shown (black lines): an isotherm at 850 °C (Fig. 3a and c) for charge–$N_2$/discharge–$CO_2$–$O_2$ protocol, and 950 °C for calcination–reduction and 800 °C for carbonation–oxidation for the charge/discharge–$CO_2$–$O_2$ protocol (Fig. 3b and d). Heating and cooling rates of 10 °C $min^{-1}$ were used in all experiments.

The behavior of $CaCO_3$ is presented in Fig. 3a and b. Complete calcination of $CaCO_3$ was achieved under both test protocols, corresponding to a 44% mass loss due to the release of $CO_2$, as expected from the thermodynamic equilibrium of the $CaCO_3$/CaO system (Fig. 2). During the carbonation stage, higher $CO_2$ uptake was obtained for the charge–$N_2$/discharge–$CO_2$–$O_2$ protocol.

The extent and kinetics of CuO reduction are strongly temperature-dependent. At the lower-temperature employed for the charge step in $N_2$ (Fig. 3c) the reduction in slow, with a total mass loss of 4.5%, well below the stoichiometric value of

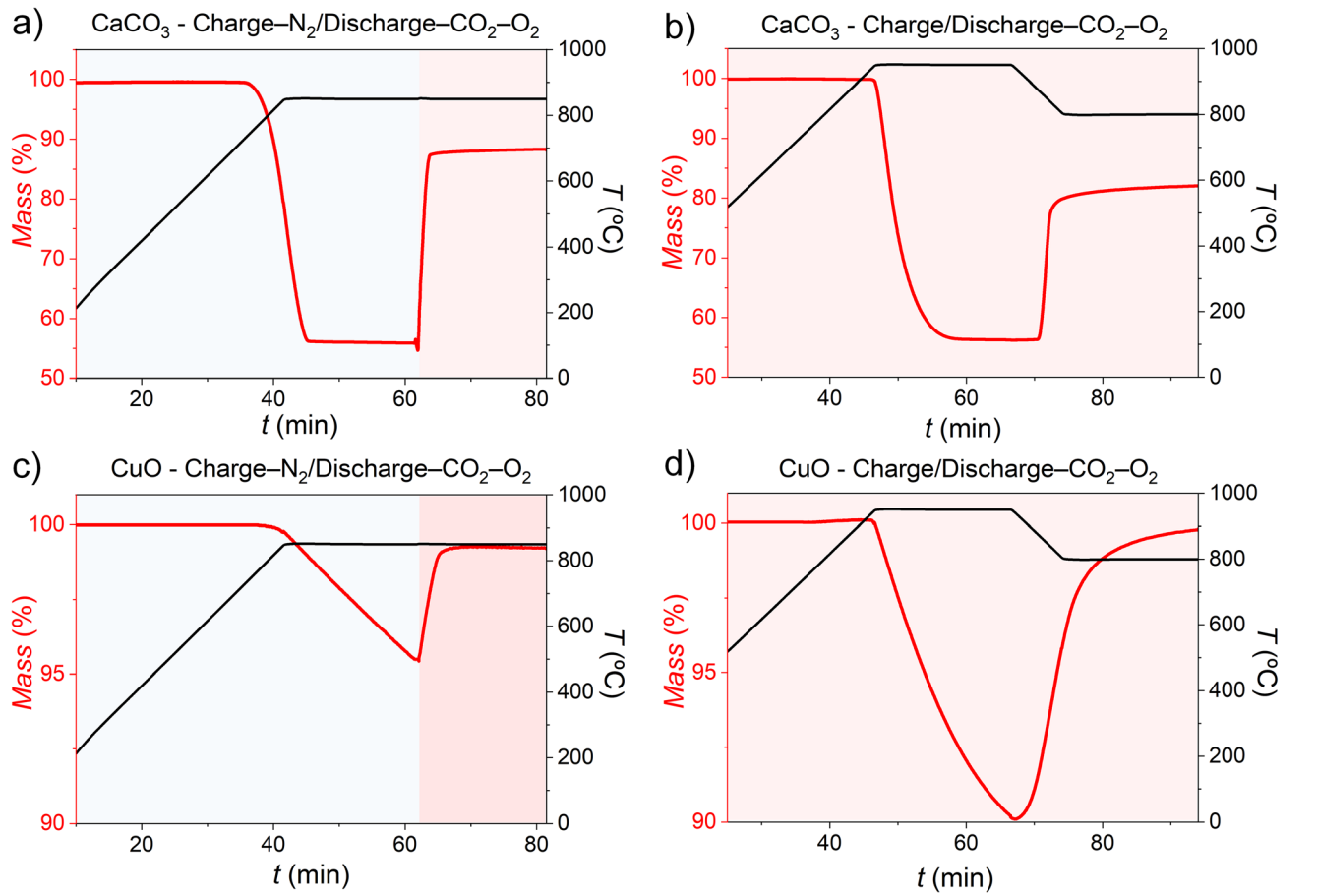


Fig. 3 Time evolution of the mass percentages (red lines) and temperature (black lines) for unmixed $CaCO_3$ (a and b) and CuO (c and d) tested under both charge–$N_2$/discharge–$CO_2$–$O_2$ and charge/discharge–$CO_2$–$O_2$ protocols. Light blue and pink shaded regions indicate $N_2$ and $CO_2$–$O_2$ atmospheres, respectively, as specified in Table 2 for both protocols.

10.01%. In contrast, complete reduction is achieved at the higher-temperature used during the charge step in a $CO_2$–$O_2$ atmosphere (Fig. 3d). As expected, the extent of subsequent oxidation is governed by the degree of the prior reduction.

The differences observed during the charging step can be attributed to kinetic limitations. Although CuO reduction is thermodynamically favored under both atmospheres, its kinetics is strongly temperature-limited. Increasing the temperature or prolonging the dwell times would increase reduction during charging in $N_2$; however, such conditions were deliberately avoided in this work, as harsher operating parameters promote sintering and deteriorate CaL performance. Overall, Fig. 3 demonstrates the feasibility of simultaneously calcining and carbonating $CaCO_3$ while coupling CuO reduction and oxidation under the experimental schemes proposed.

To investigate potential interactions between the two processes, composite samples were also tested under combined charge and discharge steps. Fig. 4 illustrates the behavior of the DCa50Cu50 material. Based on eqn (2) and (3), and considering the 50 : 50 mass ratio of this sample, the theoretical mass losses associated with $CaCO_3$ calcination and CuO reduction are 22% and 5%, respectively, yielding a total expected mass loss of 27% (eqn (5)). Experimentally, calcination occurs first and is immediately followed by CuO reduction, resulting in a two-step mass loss profile. The total mass loss was 26.5% under charge–$N_2$/discharge–$CO_2$–$O_2$ conditions and 24.7% under charge/discharge–$CO_2$–$O_2$ conditions. While complete $CaCO_3$ calcination (22%) is achieved in both operating schemes, the extent of CuO reduction depends strongly on the reaction conditions. Under charge–$N_2$/discharge–$CO_2$–$O_2$, a mass loss of 4.5% was observed, corresponding to 90% CuO reduction, whereas under charge/discharge–$CO_2$–$O_2$ the mass loss decreased to 2.7%, corresponding to a reduction degree of 54%. This behavior contrasts with that observed for pure CuO, where higher temperatures favor reduction.

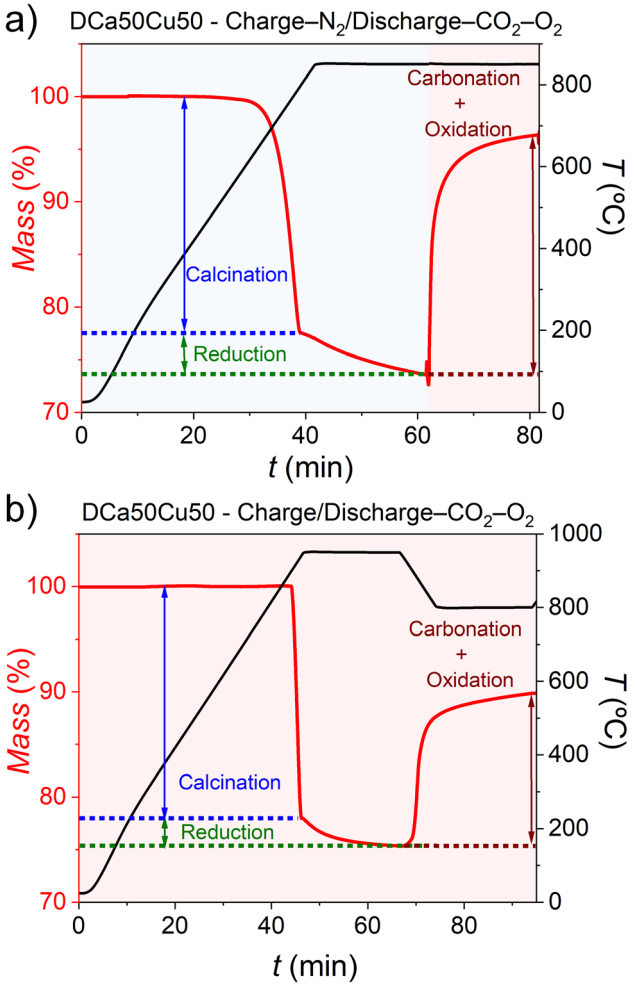


Fig. 4 Time evolution of the mass percentages (red lines) and temperature (black lines) during the first charge–discharge cycle for the sample DCa50Cu50, tested under (a) charge–$N_2$/discharge–$CO_2$–$O_2$ and (b) charge/discharge–$CO_2$–$O_2$ conditions. Light blue and pink shaded regions indicate $N_2$ and $CO_2$–$O_2$ atmospheres, respectively, as specified in Table 2 for both protocols.

This apparent discrepancy suggests that additional factors, beyond the intrinsic thermodynamics of the CuO/$Cu_2O$ system, govern the reactivity within the composite. In particular, under more severe conditions, the interaction between CaO and CuO at high temperature leads to the formation of mixed phases, as will be discussed in Section 3.5 where XRD analysis shows the formation of mixed oxides, which affect the effective availability and reactivity of Cu species during the reduction step. As a result, despite the higher temperatures, the extent of CuO reduction is hindered compared to that observed under milder conditions.

During the discharge step, carbonation and oxidation occur simultaneously and therefore cannot be individually resolved from the mass evolution curves. However, the total conversion (eqn (4)) can be directly determined. The individual conversions of CaO and $Cu_2O$ were estimated from eqn (6) and (7) using the subsequent calcination–reduction step. Despite the isothermal conditions, the mass loss curve exhibits two distinguishable stages: an initial rapid mass loss associated with $CaCO_3$ calcination, followed by a second stage corresponding to CuO reduction. This sequential behavior enables the estimation of the corresponding contributions, assuming that the species formed during discharge are fully converted back during the charge step.

### 3.2. Influence of the $CaCO_3$/CuO mass ratio and the mixing procedure on multicycle performance

Fig. 5 shows the time evolution of the mass percentages and temperature, and the corresponding total conversions at each $N$ cycle, $X_{T,N}$, calculated from eqn (4), for the composites DCa95Cu05, DCa80Cu20, and DCa50Cu50 tested under charge–$N_2$/discharge–$CO_2$–$O_2$ conditions for 20 cycles.

The Ca-rich samples (DCa95Cu05 and DCa80Cu20) show a rapid decay in mass gain associated with carbonation–oxidation as the cycles progress (Fig. 5a–d), with the effect being most pronounced for DCa95Cu05. Consequently, reactivity decreases sharply and, although it stabilizes after 12 cycles, total conversion remains very low, reaching only 0.07 by the twentieth cycle. DCa80Cu20 exhibits improved performance during the initial

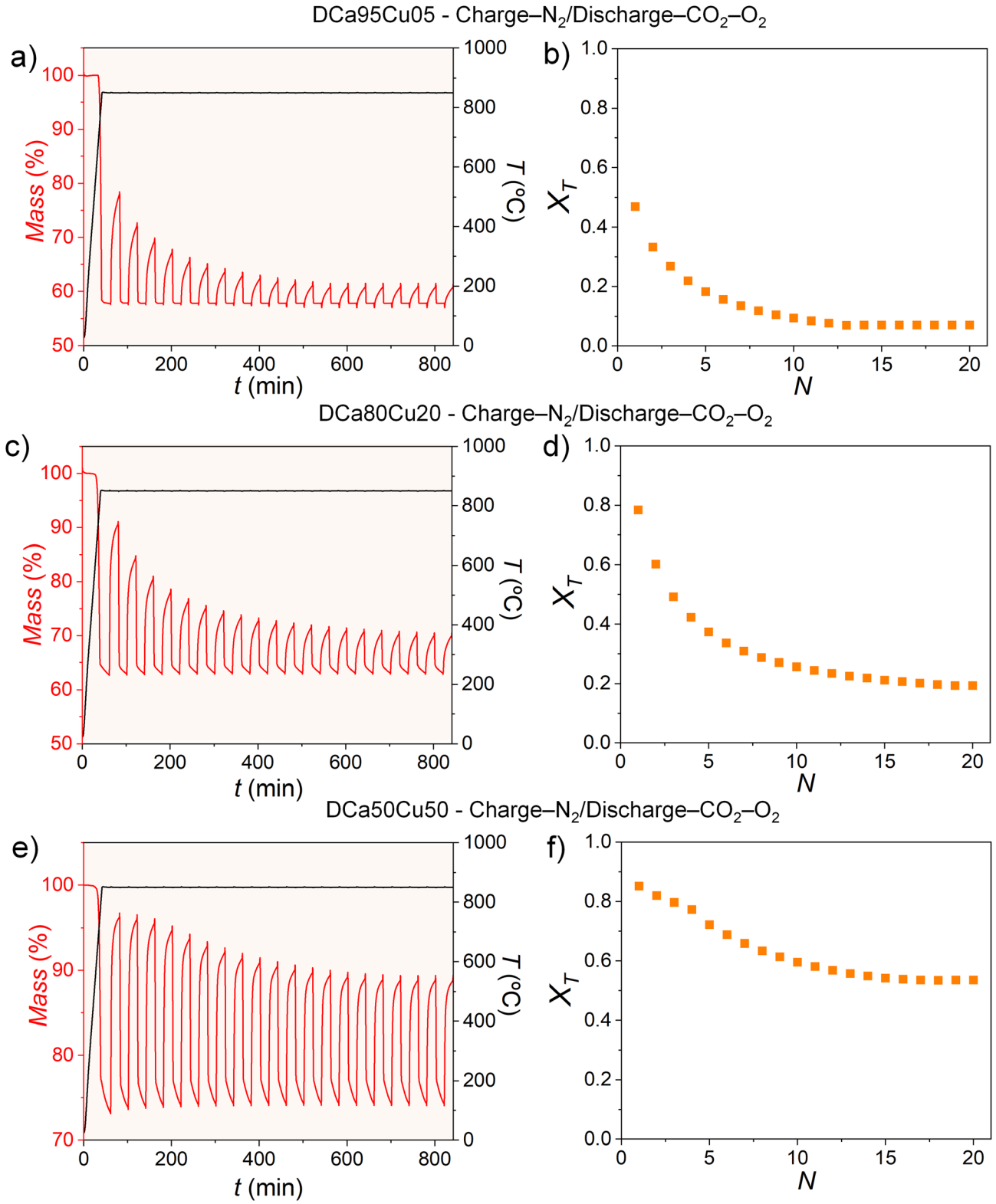


Fig. 5 Time evolution of the % mass and corresponding total conversions ($X_{T,N}$) for the samples (a and b) DCa95Cu05, (c and d) DCa80Cu20, and (e and f) DCa50Cu50 tested under charge–$N_2$/discharge–$CO_2$–$O_2$ conditions.

cycles; however, a significant decline in mass gain is observed from cycle 5 onwards, leading to total conversion values that stabilize after 16 cycles at around 0.19.

In contrast, DCa50Cu50 maintains a high mass gain throughout the 20 cycles, resulting in sustained total conversion values in the range of 0.85–0.54 (Fig. 5e and f).

These results demonstrate that low CuO contents are detrimental to cyclic performance, whereas a near-equimass $CaCO_3$–CuO composition is critical for preserving long-term reactivity of the composite materials.

Based on these findings and prior literature reports showing that milling modifies the microstructure of Ca-based materials and, consequently, their multicycle performance,[53,54] 50 : 50 composites were prepared using wet ball milling (WCa50Cu50) and freeze granulation (FCa50Cu50) for comparison with the dry-milled DCa50Cu50 sample. Under charge–$N_2$/discharge–$CO_2$–$O_2$ conditions (Fig. 6), WCa50Cu50 exhibits cyclic behavior comparable to that of DCa50Cu50, with total conversion values in the range 0.80–0.47. In contrast, FCa50Cu50 shows a lower initial performance but progressively stabilizes to similar conversion levels as the cycles progress ($X_T = 0.73$–$0.46$). Overall, these results confirm that the 50 : 50 $CaCO_3$–CuO composition yields superior multicycle performance, while the mixing method modulates the attainable activity levels.

### 3.3. Influence of the test conditions on the multicycle performance

On the basis of their superior performance, DCa50Cu50, WCa50Cu50, and FCa50Cu50 were tested under the more severe charge/discharge–$CO_2$–$O_2$ protocol (20 cycles) and their behavior was compared with that observed under charge–$N_2$/discharge–$CO_2$–$O_2$ (Fig. 7).

The extent of deactivation strongly depends on both operating conditions and sample history. For example, DCa50Cu50 (Fig. 7a and b) exhibits higher reactivity under charge–$N_2$/discharge–$CO_2$–$O_2$ conditions, as the lower calcination/reduction temperatures (under $N_2$) partially suppress sintering.

By contrast, the charge/discharge–$CO_2$–$O_2$ protocol imposes harsher conditions, combining higher temperatures with elevated $CO_2$ partial pressure, which promote sintering during calcination. This process generally leads to increased crystallinity, pore coarsening and concomitant reduction in the specific surface area for carbonation.[28] In addition, sintering also promotes particle agglomeration, which diminishes the oxidation extent of $Cu_2O$.[44]

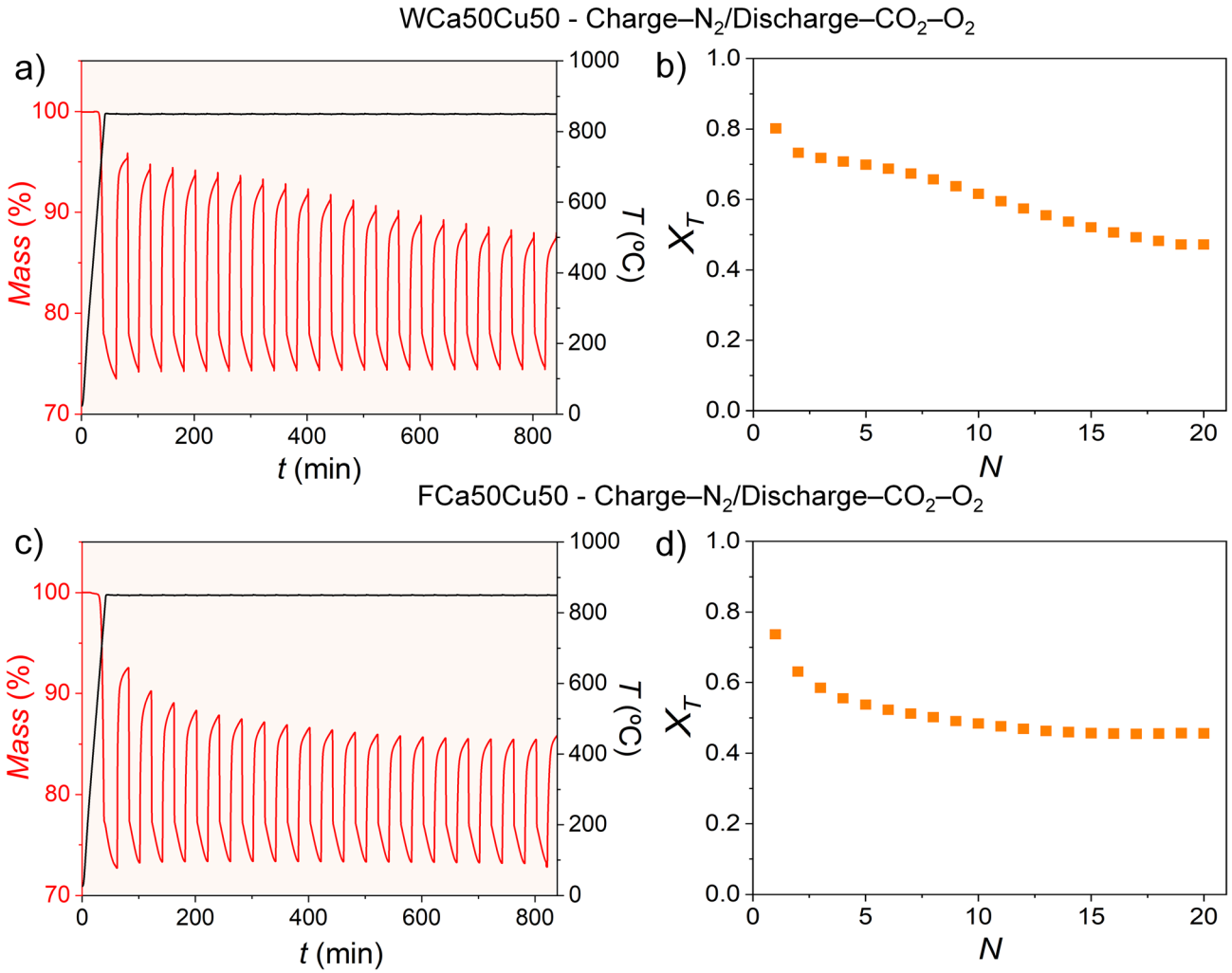


Fig. 6 Time evolution of the % mass and corresponding total conversions ($X_{T,N}$) for the samples (a and b) WCa50Cu50 and (c and d) FCa50Cu50, tested under charge–$N_2$/discharge–$CO_2$–$O_2$ conditions.

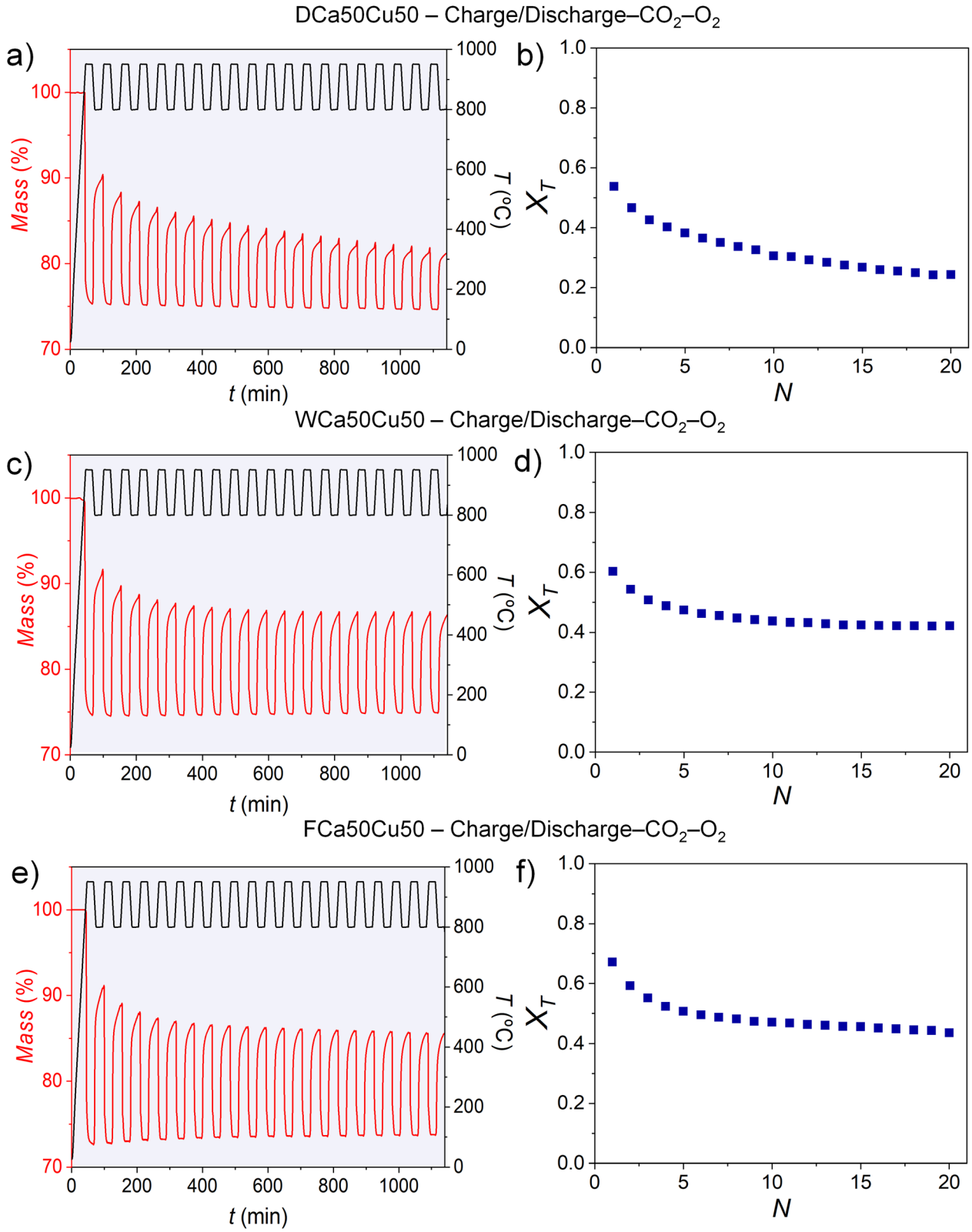


Fig. 7 Time evolution of the % mass and corresponding total conversions ($X_{T,N}$) for the samples (a and b) DCa50Cu50, (c and d) WCa50Cu50, and (e and f) FCa50Cu50 tested under charge/discharge–$CO_2$–$O_2$ conditions.

Interestingly, under charge/discharge–$CO_2$–$O_2$ conditions, the preparation method exert a strong influence on reactivity. In this context, WCa50Cu50 (Fig. 7c and d) exhibits a higher and more stable mass gain, which is also reflected in the total conversion, compared to DCa50Cu50. This behavior suggests that low-energy wet milling produces structures less prone to

 

sintering at high temperatures. This interpretation is consistent with previous reports indicating that high-energy Emax milling produces bimodal particle-size distributions and ultrafine crystallites that, although beneficial under mild cycling conditions, are more susceptible to sintering under aggressive thermal/$CO_2$ conditions.[53]

FCa50Cu50 (Fig. 7e and f) shows reactivity comparable to that of WCa50Cu50, reinforcing the conclusion that the sample preparation route significantly affects multicycle performance under severe charge/discharge–$CO_2$–$O_2$ conditions.

### 3.4. CaO and $Cu_2O$ conversions and energy storage density

To facilitate comparison, detailed values of conversions ($X_{CaO}$ and $X_{CuO}$) and energy storage densities ($D_m$) at cycles 1 and 20 are provided in Tables 3 and 4 for charge–$N_2$/discharge–$CO_2$–$O_2$ and charge/discharge–$CO_2$–$O_2$ protocols, respectively. This section highlights principal trends and representative values.

Overall, all 50 : 50 composites deliver higher total energy densities than the individual components under at least one operating protocol, while the relative contribution of CaO and $Cu_2O$ depends on both preparation and cycling conditions.

Fig. 8 shows the conversions (eqn (6) and (7)) and cycle-resolved energy storage densities (eqn (8) and (9)) of the individual components CaO and $Cu_2O$, calculated from thermogravimetric data recorded under charge–$N_2$/discharge–$CO_2$–$O_2$ conditions (Fig. S1, SI).

Pure CaO shows high initial conversion that declines and stabilizes at low values after the first few cycles (Fig. 8a and b). This multicycle behavior is consistent with previously published results for samples of identical particle size tested under comparable conditions.[55]

In contrast, $Cu_2O$ shows low initial conversion due to incomplete reduction; however, the conversion stabilizes as cycling proceeds (Fig. 8c and d, see also Table 3).

Fig. 9 shows the conversions and energy storage densities for the composites tested under charge–$N_2$/discharge–$CO_2$–$O_2$ conditions, together with the percentage contribution of each component to the total stored energy.

For the DCa50Cu50 composite, CaO exhibits very high initial conversion with only a moderate decline by cycle 20, whereas the $Cu_2O$ conversion remains moderate and stable. Therefore, CaO provides the dominant contribution to the stored energy. The total energy density, $D_m$, although decreases with the number of cycles, still retains significant capacity in the final cycles (Fig. 9a, b and Table 3).

A different behavior is observed for WCa50Cu50. The CaO conversion is somewhat lower than in DCa50Cu50, suggesting that dry ball milling of $CaCO_3$ in the Emax mill is more beneficial for the subsequent reactivity of CaO than wet ball milling. The positive effect of Emax milling of $CaCO_3$ on thermochemical energy storage has been previously reported for pure $CaCO_3$ samples.[53] In contrast, the $Cu_2O$ conversion is higher and more stable over cycling. Wet mixing therefore enhances $Cu_2O$ reactivity and shifts the energy contribution toward the CuO/$Cu_2O$ system (Fig. 9c, d and Table 3).

Finally, FCa50Cu50 exhibits a reduced CaO conversion but the highest $Cu_2O$ conversion among the composites, resulting in a larger fraction of the stored energy being provided by the redox component (Fig. 9e, f and Table 3).

Table 3 Conversions ($X$) and energy storages densities ($D_m$, in MJ $kg^{-1}$) of the samples tested under charge–$N_2$/discharge–$CO_2$–$O_2$ conditions. Values are reported for the first cycle ($N = 1$) and the twentieth cycle ($N = 20$). Data also include the percentage contribution of each component to the total energy storage, and the total $D_m$

| | | Charge–$N_2$/discharge–$CO_2$–$O_2$ | |
|---|---|---|---|
| Sample | Parameter | $N = 1$ | $N = 20$ |
| $CaCO_3$ | $X_{CaO}$ | 0.76 | 0.24 |
| | $D_{m,CaO}$ | 2.42 | 0.75 |
| CuO | $X_{Cu_2O}$ | 0.07 | 0.44 |
| | $D_{m,Cu_2O}$ | 0.06 | 0.40 |
| DCa50Cu50 | $X_{CaO}$ | 0.89 | 0.53 |
| | $D_{m,CaO}$ (contrib. (%)) | 2.84 (83%) | 1.70 (17%) |
| | $X_{Cu_2O}$ | 0.66 | 0.54 |
| | $D_{m,Cu_2O}$ (contrib. (%)) | 0.60 (78%) | 0.49 (22%) |
| | $D_{m,T}$ | 3.44 | 2.19 |
| WCa50Cu50 | $X_{CaO}$ | 0.79 | 0.43 |
| | $D_{m,CaO}$ (contrib. (%)) | 2.52 (77%) | 1.37 (23%) |
| | $X_{Cu_2O}$ | 0.83 | 0.65 |
| | $D_{m,Cu_2O}$ (contrib. (%)) | 0.76 (70%) | 0.59 (30%) |
| | $D_{m,T}$ | 3.28 | 1.96 |
| FCa50Cu50 | $X_{CaO}$ | 0.69 | 0.39 |
| | $D_{m,CaO}$ (contrib. (%)) | 2.19 (72%) | 1.24 (65%) |
| | $X_{Cu_2O}$ | 0.93 | 0.74 |
| | $D_{m,Cu_2O}$ (contrib. (%)) | 0.84 (28%) | 0.66 (35%) |
| | $D_{m,T}$ | 3.03 | 1.90 |

Table 4 Conversions ($X$) and energy storages densities ($D_m$, in MJ $kg^{-1}$) of the samples tested under charge/discharge–$CO_2$–$O_2$ conditions. Values are reported for the first cycle ($N = 1$) and the twentieth cycle ($N = 20$). Data also include the percentage contribution of each component to the total energy storage, and the total $D_m$

| | | Charge/discharge–$CO_2$–$O_2$ | |
|---|---|---|---|
| Sample | Parameter | $N = 1$ | $N = 20$ |
| $CaCO_3$ | $X_{CaO}$ | 0.61 | 0.20 |
| | $D_{m,CaO}$ | 1.94 | 0.62 |
| CuO | $X_{Cu_2O}$ | 0.95 | 0.92 |
| | $D_{m,Cu_2O}$ | 0.86 | 0.83 |
| DCa50Cu50 | $X_{CaO}$ | 0.55 | 0.23 |
| | $D_{m,CaO}$ (contrib. (%)) | 1.74 (80%) | 0.72 (72%) |
| | $X_{Cu_2O}$ | 0.50 | 0.32 |
| | $D_{m,Cu_2O}$ (contrib. (%)) | 0.45 (20%) | 0.29 (28%) |
| | $D_{m,T}$ | 2.19 | 1.01 |
| WCa50Cu50 | $X_{CaO}$ | 0.62 | 0.39 |
| | $D_{m,CaO}$ (contrib. (%)) | 1.97 (80%) | 1.23 (71%) |
| | $X_{Cu_2O}$ | 0.53 | 0.59 |
| | $D_{m,Cu_2O}$ (contrib. (%)) | 0.48 (20%) | 0.51 (29%) |
| | $D_{m,T}$ | 2.45 | 1.74 |
| FCa50Cu50 | $X_{CaO}$ | 0.68 | 0.41 |
| | $D_{m,CaO}$ (contrib. (%)) | 2.15 (79%) | 1.29 (72%) |
| | $X_{Cu_2O}$ | 0.65 | 0.56 |
| | $D_{m,Cu_2O}$ (contrib. (%)) | 0.59 (21%) | 0.51 (28%) |
| | $D_{m,T}$ | 2.74 | 1.80 |

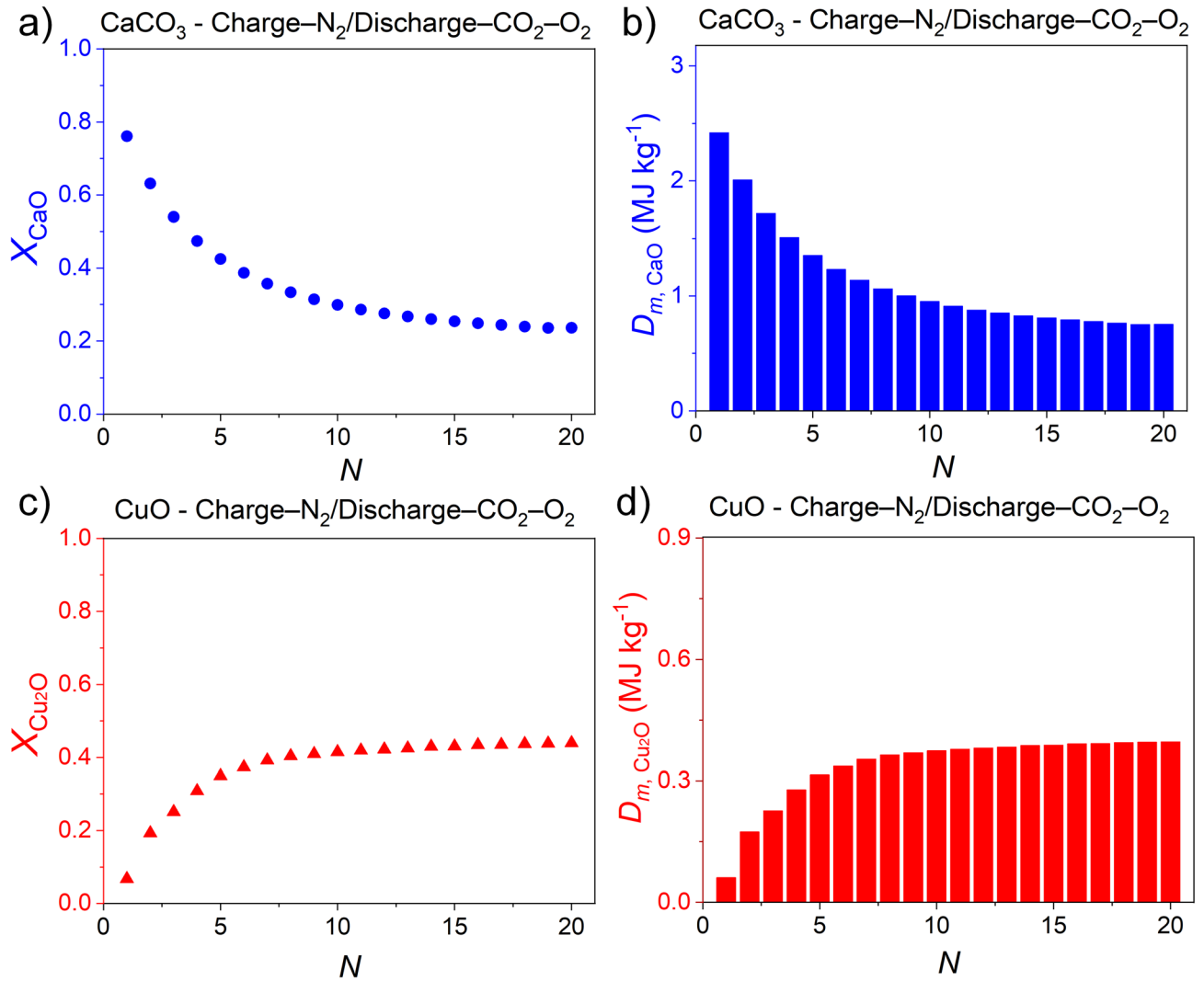


Fig. 8 Conversions ($X$) and energy storage densities ($D_m$) as a function of the cycle number for the starting components of the composites tested under charge–$N_2$/discharge–$CO_2$–$O_2$ conditions: (a and b) CaO, and (c and d) $Cu_2O$.

Overall, the preparation route strongly influences the reactivity, and thus the energy storage density, of each component. Importantly, all composites outperform the pure starting materials in terms of total stored energy, $D_m$ (Table 3).

Fig. 10 presents the conversions and energy storage densities of the starting components of the composites tested under the harsher charge/discharge–$CO_2$–$O_2$ protocol, as obtained from the thermogravimetric cycling data (Fig. S2, SI).

The $CaCO_3$/CaO pair suffers a marked and progressive loss of reactivity with cycle number, a behavior commonly attributed to thermally driven sintering and pore coarsening that reduce the surface area available for carbonation (Fig. 10a and b). This result is consistent with previously reported data for samples tested under comparable conditions.[55]

In contrast, the CuO/$Cu_2O$ redox pair benefits from the higher charge temperatures (Fig. 10c and d), which favor more complete reduction and sustain reactivity over repeated cycles (Table 4).

When these components are combined in composites, the overall performance reflects the interplay between these opposing tendencies and the preparation route (Fig. 11). DCa50Cu50, prepared by high-energy dry milling, shows a higher initial contribution from CaO but a more pronounce loss of activity under severe conditions, consistent with enhanced sintering (Fig. 11a and b). WCa50Cu50, produced by wet milling, exhibits a more balanced behavior in which $Cu_2O$ remains highly active, resulting in more stable conversion upon cycling, while CaO presents higher reactivity from the first cycle than in the previous case (Fig. 11c and d). FCa50Cu50, obtained by freeze granulation, shows reactivity similar to WCa50Cu50, together with a noticeable enhancement of the $Cu_2O$ contribution relative to DCa50Cu50 (Fig. 11e and f).

In all cases, the combined systems also deliver total $D_m$ values that exceed the energy storage densities of the individual components tested separately, as both thermochemical subsystems contribute usable energy. Moreover, particularly in WCa50Cu50 and FCa50Cu50, the coexistence of the two phases

 

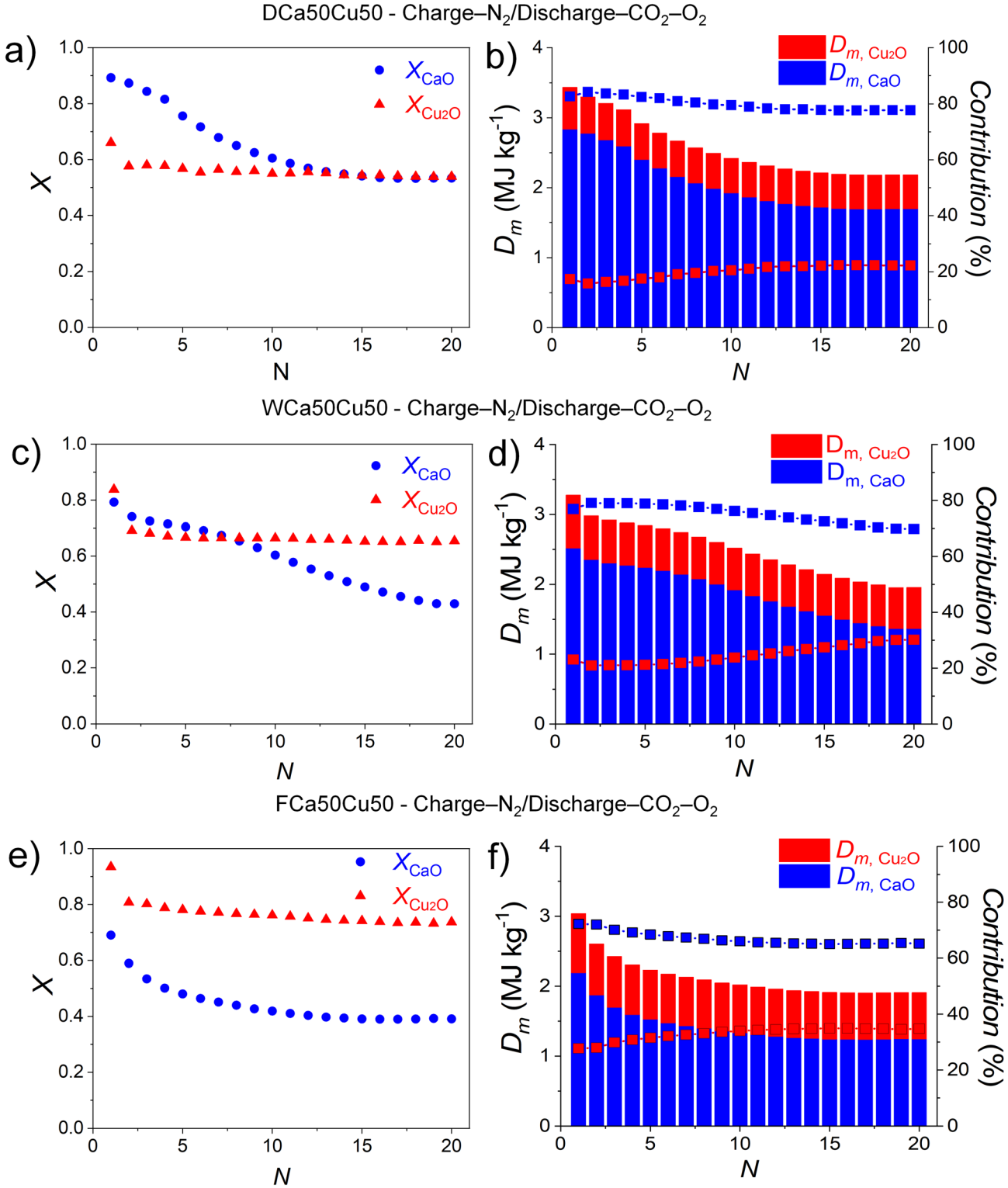


Fig. 9 Conversions ($X$) and energy storage densities ($D_m$) for CaO and $Cu_2O$ as a function of the cycle number for samples (a and b) DCa50Cu50, (c and d) WCa50Cu50, and (e and f) FCa50Cu50 tested under charge–$N_2$/discharge–$CO_2$–$O_2$ conditions.

appears to partially mitigate the reactivity decay of each component. Overall, these observations indicate that although severe operating conditions thermodynamically favor $Cu_2O$ reactivity, the practical long-term energy output also depends critically on the preparation method (Table 4).

To evaluate the long-term viability of each sample, the cumulative energy storage density over 20 cycles was quantified by integrating the cycle-resolved data (Fig. 12). This analysis confirms that all composites outperform the individual $CaCO_3$ and CuO materials under both mild (charge–$N_2$/discharge–

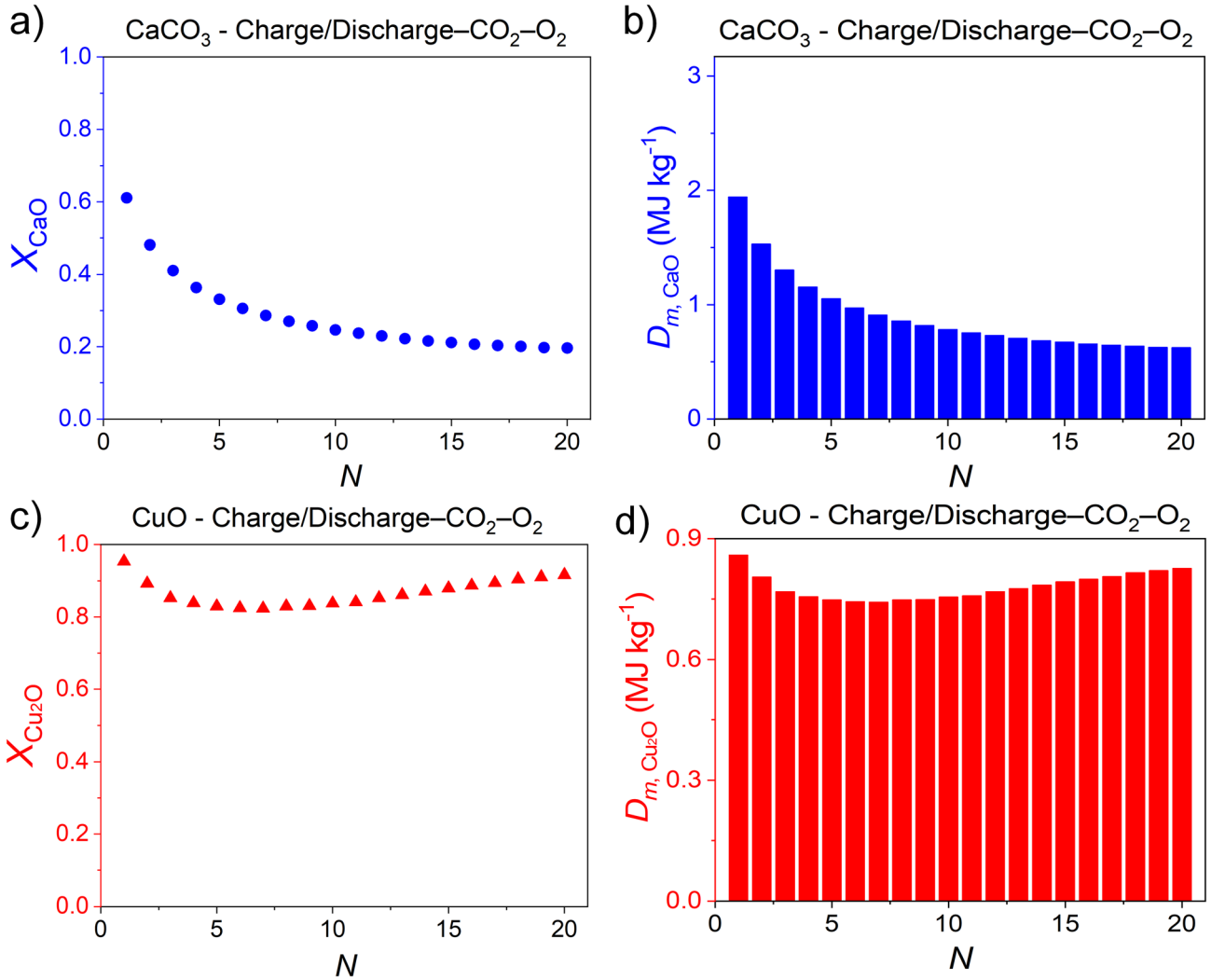


Fig. 10 Conversions ($X$) and energy storage densities ($D_m$) as a function of the cycle number for the starting components of the composites tested under charge/discharge–$CO_2$–$O_2$ conditions: (a and b) CaO and (c and d) $Cu_2O$.

$CO_2$–$O_2$) and severe (charge/discharge–$CO_2$–$O_2$) conditions, although the extent of the improvement depends on the preparation method and the operating conditions.

A quantitative comparison highlights the magnitude of this improvement. Under mild conditions, the accumulated energy density increases from 20.9 MJ $kg^{-1}$ for $CaCO_3$ and 6.51 MJ $kg^{-1}$ for CuO to 47.07 MJ $kg^{-1}$ for the WCa50Cu50 composite. Similarly, under severe conditions, the energy density increases from 16.79 MJ $kg^{-1}$ ($CaCO_3$) and 14.78 MJ $kg^{-1}$ (CuO) to 35.46 MJ $kg^{-1}$ for WCa50Cu50. These results demonstrate that the incorporation of CuO into the $CaCO_3$/CaO system introduces an additional and significant contribution to energy storage through the CuO/$Cu_2O$ redox couple.

Considering all results, including conversions, cycle-resolved energy storage densities, and accumulated energy values, WCa50Cu50 stands out as the most robust candidate due to its balanced performance across both operating conditions. Under mild conditions, it clearly outperforms FCa50Cu50 and matches the performance of DCa50Cu50, combining high CaO conversion with enhanced $Cu_2O$ activity and exhibiting slower deactivation. Under severe conditions, although FCa50Cu50 shows a marginal advantage in $Cu_2O$ reactivity, its performance drop under mild conditions makes it less versatile. Moreover, under these severe conditions, while DCa50Cu50 excels initially, it suffers the most pronounced deactivation.

Consequently, WCa50Cu50 was selected for further structural, morphological, optical and thermal characterization, as it provides the best overall balance between efficiency and multicycle stability for thermochemical energy storage.

### 3.5. Structural, optical, thermal and microstructural characterization

The WCa50Cu50 composite, identified as the optimal formulation for multicycle energy storage, was subjected to comprehensive characterization to correlate its structural, optical, thermal and morphological properties with its robust performance under both mild and severe operating conditions.

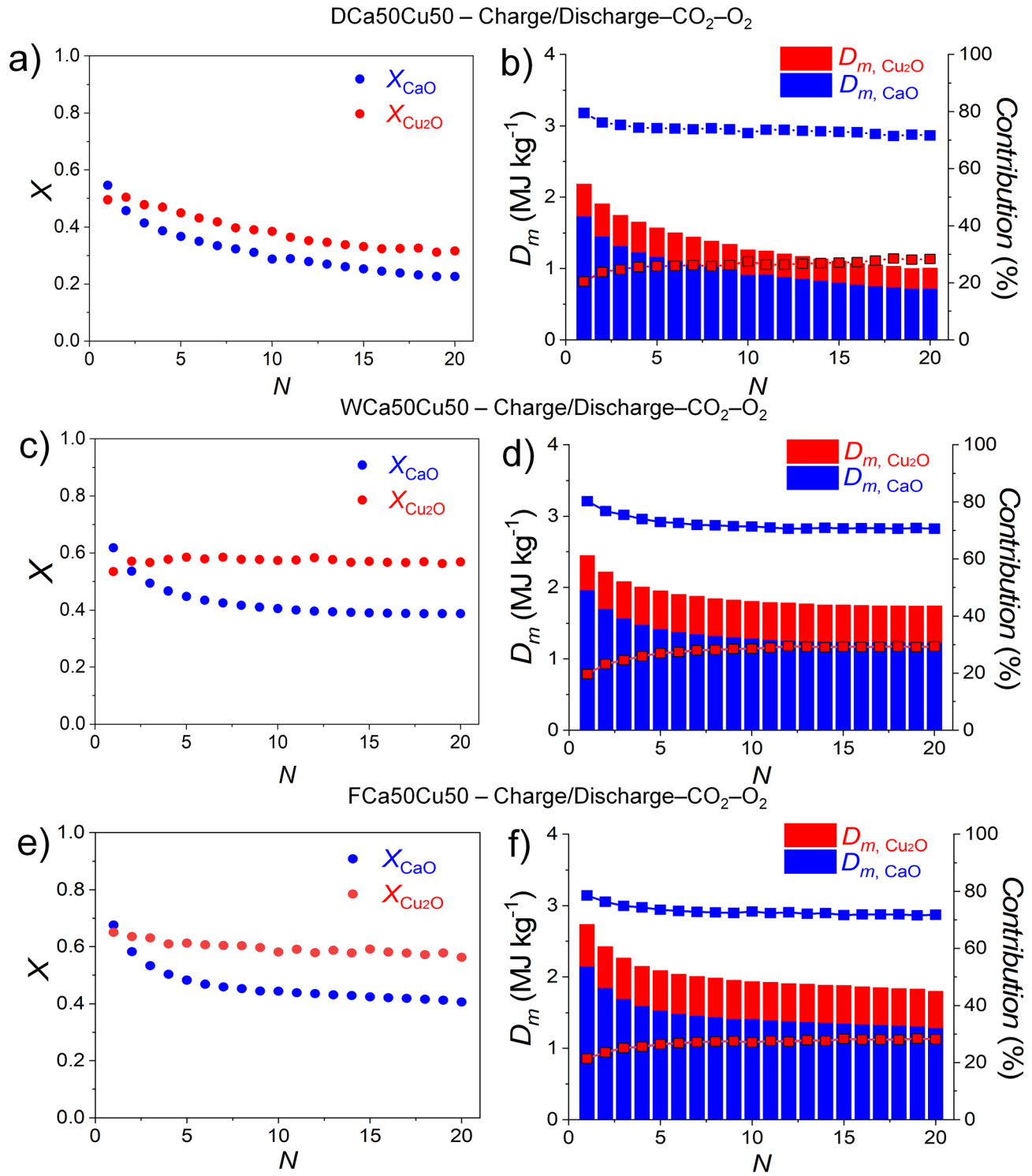


Fig. 11 Conversions ($X$) and energy storage densities ($D_m$) for CaO and $Cu_2O$ as a function of the cycle number for samples (a and b) DCa50Cu50, (c and d) WCa50Cu50, and (e and f) FCa50Cu50 tested under charge/discharge–$CO_2$–$O_2$ conditions.

X-ray diffraction (XRD) patterns were recorded at room temperature for the as prepared sample and after 20 cycles (ending in the discharge step) under mild, charge–$N_2$/discharge–$CO_2$–$O_2$, and severe, charge/discharge–$CO_2$–$O_2$, conditions. The XRD pattern of the as-prepared sample (Fig. 13a) displays the characteristic diffraction peaks of the precursors, calcium carbonate ($CaCO_3$) and copper oxide (CuO). Upon cycling under mild conditions (Fig. 13b), diffraction peaks attributable to $Ca_2CuO_3$ emerge, indicating the formation

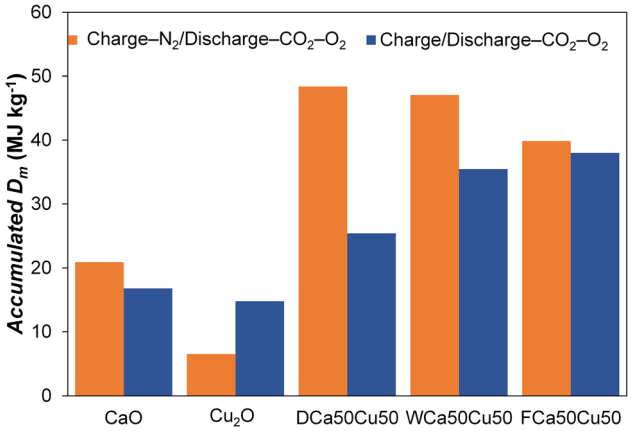


Fig. 12 Accumulated energy density over 20 cycles for CaO, $Cu_2O$, and the 50 : 50 composites under mild charge–$N_2$/discharge–$CO_2$–$O_2$ and severe charge/discharge–$CO_2$–$O_2$ conditions.

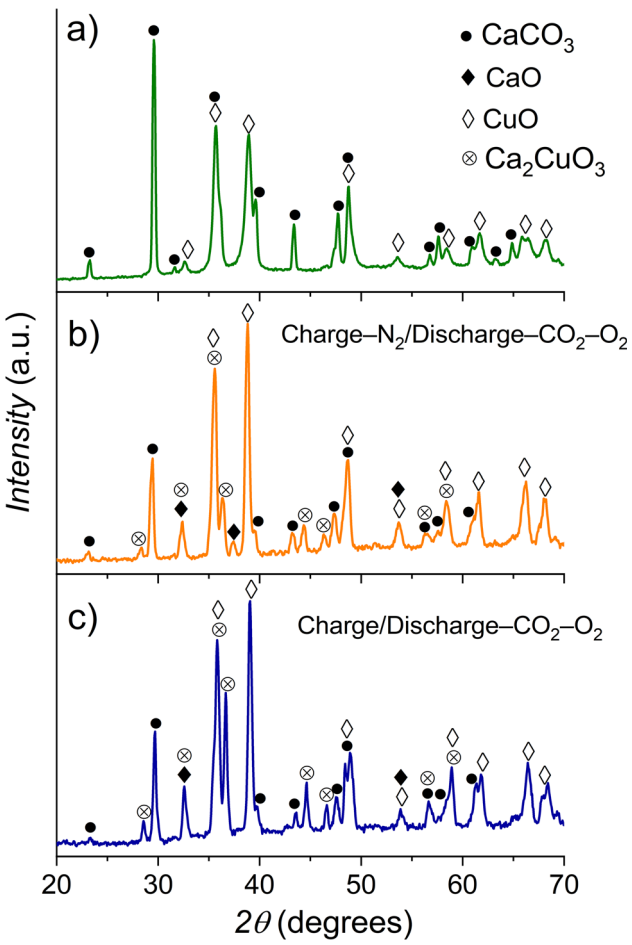


Fig. 13 X-ray diffraction patterns of the composite WCa50Cu50: (a) as prepared, (b) after 20 cycles under charge–$N_2$/discharge–$CO_2$–$O_2$ conditions, and (c) after 20 cycles under charge/discharge–$CO_2$–$O_2$ conditions.

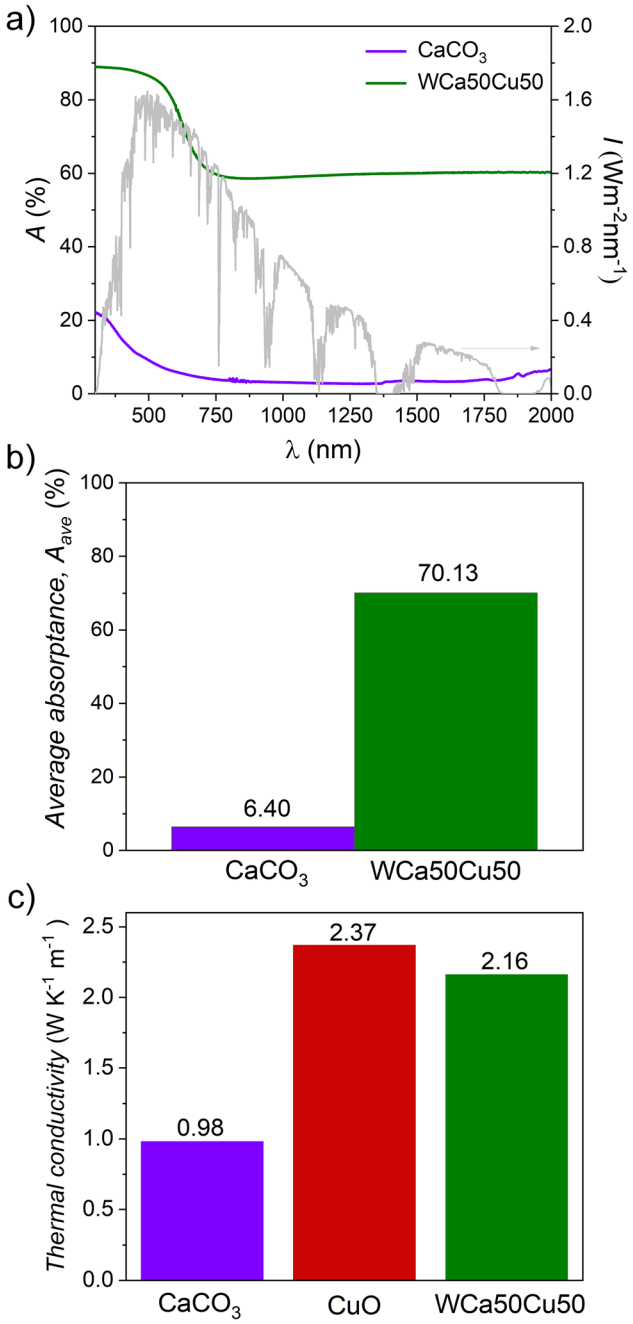


Fig. 14 (a) Spectral absorptance of WCa50Cu50 (green line) and $CaCO_3$ (violet line), and spectral irradiance of sunlight reaching the Earth's surface (AM1.5G). (b) Average solar absorptance of WCa50Cu50 and limestone, calculated from eqn (12). (c) Thermal conductivities of $CaCO_3$, CuO and WCa50Cu50, measured at 400 °C.

of this phase during successive high-temperature charge/discharge cycles from CaO and CuO.

Similar phases are also observed under severe conditions (Fig. 13c), although the relative intensities of the diffraction peaks suggest a higher abundance of $Ca_2CuO_3$ under these conditions. While the formation of $Ca_2CuO_3$ could, in principle, reduce the availability of CaO and CuO for the carbonation and redox reactions, *in situ* XRD studies have shown that this phase decomposes at high temperatures under reducing or $CO_2$ atmospheres, regenerating the active phases or forming $CaCO_3$, respectively.[56–58] Therefore, $Ca_2CuO_3$ can be considered

 

a functionally reversible phase under the experimental conditions of this work.

However, the combined analysis of XRD and thermogravimetric results suggests that its transient formation influences the thermochemical performance. The higher relative abundance of $Ca_2CuO_3$ under severe conditions correlates with the lower extent of CuO reduction observed under these conditions, indicating that this phase affects the reactivity of the system during cycling.

The spectral absorptance $A(\lambda)$ measurements were performed using a UV-Vis-NIR spectrophotometer, and was calculated according to eqn (11):

$$A(\lambda) = 100\% - R(\lambda) \tag{11}$$

where $\lambda$ is the wavelength of the incident radiation and $R(\lambda)$ is the reflectance in %. From these data, the average solar absorptance was subsequently obtained using eqn (12):

$$A = \frac{\int_{300\ \mathrm{nm}}^{2000\ \mathrm{nm}} A(\lambda) I(\lambda) \mathrm{d}\lambda}{\int_{300\ \mathrm{nm}}^{2000\ \mathrm{nm}} I(\lambda) \mathrm{d}\lambda} \tag{12}$$

where $I(\lambda)$ is the AM1.5G spectral solar irradiance. Fig. 14a compares the spectral absorptance of the WCa50Cu50 composite (green line) with that of the pure natural limestone sample ($CaCO_3$, violet line). While limestone exhibits very low absorptance across the entire solar spectrum, with values well below 25% and an average solar absorptance of only 6.40% (Fig. 14b), the composite reaches absorptance values between 60% and 90% across the solar spectrum, yielding an average solar absorptance of 70.13%. This corresponds to a tenfold enhancement over pure limestone, primarily driven by the high intrinsic absorptivity of the CuO phase. Such a substantial improvement highlights the strong potential of this composite for direct solar absorption in thermochemical energy storage receivers.[24,31,59]

Regarding thermal transport (Fig. 14c), the thermal conductivity increases from 0.98 W $K^{-1}$ $m^{-1}$ for $CaCO_3$ to 2.16 W $K^{-1}$ $m^{-1}$ for the composite at 400 °C, corresponding to more than a twofold enhancement. This value approaches that of pure CuO (2.37 W $K^{-1}$ $m^{-1}$). These results suggest that the incorporation of CuO promotes the formation of a more efficient heat transfer network within the $CaCO_3$ matrix. From a TCES perspective, this improvement is particularly relevant, as it enhances heat transfer during both the charging and discharging steps, reduces thermal gradients within the material, promotes more homogeneous reactivity, and mitigates local overheating effects.

Scanning electron microscopy (SEM) was employed to examine the microstructural features of the WCa50Cu50 composite and to assess the morphological transformations induced by cyclic operation under mild and severe conditions. The analysis aims to stablish qualitative correlations between microstructure, preparation route, and the observed multicycle performance. Representative SEM images of the as-prepared material and of the samples after the thermochemical testing, ending in the carbonation step, are shown in Fig. 15. Elemental distribution was analyzed by EDX mapping to evaluate possible phase segregation effects induced by cycling.

The as-prepared WCa50Cu50 composite (Fig. 15a) exhibits a heterogeneous but intermixed morphology, in which $CaCO_3$

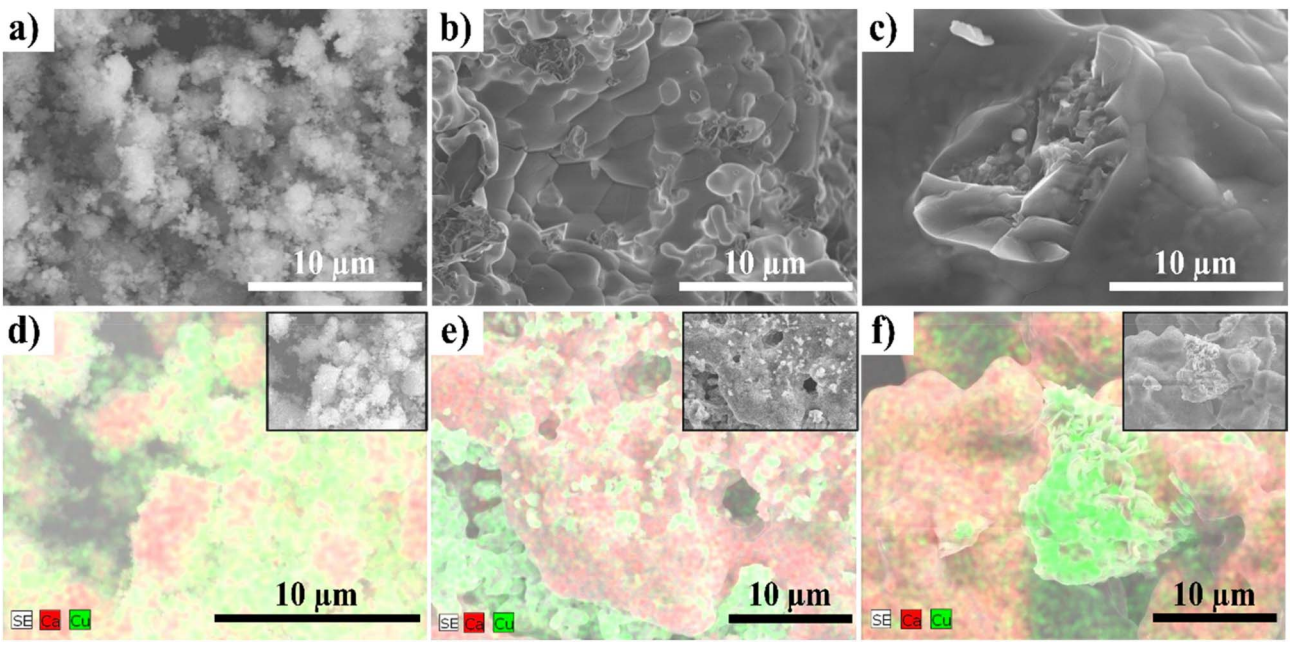


Fig. 15 SEM images and corresponding EDX elemental maps of the WCa50Cu50 composite: (a and d) as-prepared sample. (b and e) Sample after 20 cycles under charge–$N_2$/discharge–$CO_2$–$O_2$ conditions, ending in the discharge step. (c and f) Sample after 20 cycles under charge/discharge–$CO_2$–$O_2$ conditions, ending in the discharge step.

and CuO particles are intimately distributed. The wet milling route effectively produces $CaCO_3$ aggregates decorated with nanometric CuO particles, ensuring a high contact area between phases. This observation is confirmed by EDX elemental maps, which show a relatively homogeneous spatial distribution of Ca and Cu throughout the analyzed area (Fig. 15d). Such intimate mixing is consistent with the enhanced reactivity of the composite, with balanced CaO and $Cu_2O$ contributions to the overall performance.

After 20 cycles under mild conditions (Fig. 15b), the microstructure evolves into distinguishable $CaCO_3$ patches and localized Cu-rich regions. Despite this slight elemental redistribution (Fig. 15e), a significant degree of phase intermixing is preserved, correlating with the low deactivation rates observed.

In contrast, the severe protocol (Fig. 15c) triggers conspicuous sintering and densification. EDX maps (Fig. 15f) reveal more pronounced phase separation, explaining the sharper decline in CaO reactivity. Nevertheless, the $CuO/Cu_2O$ activity remains resilient, sustained by the robust nature of the composite framework.

Overall, the combined SEM and EDX analyses confirm that the wet milling preparation yields a robust microstructure that maintains sufficient homogeneity to sustain balanced thermochemical performance, even under aggressive cycling conditions.

# 4. Conclusions

The feasibility of a hybrid thermochemical energy storage system integrating calcium-looping and Cu-based redox reactions has been demonstrated. The proposed system is based on $CaCO_3$ as a CaO precursor for calcium-looping and CuO as a $Cu_2O$ precursor for a redox reaction.

Operating conditions enabling the concurrent progress of both reaction schemes were optimized through two different approaches. Under charge–$N_2$/discharge–$CO_2$–$O_2$ conditions, cycling was driven by atmosphere switching at 850 °C. Alternatively, under charge/discharge–$CO_2$–$O_2$ conditions, cycling was induced by temperature variation at constant gas composition. Although the latter approach requires higher discharge temperatures and thus harsher operation, it eliminates the need for gas separation in CSP applications, representing a potential process-level advantage.

The CuO content critically influenced system performance. Low CuO loadings (5 and 20% mass) resulted in significant deactivation toward carbonation and oxidation. In contrast, a 50 : 50 $CaCO_3$/CuO mass ratio provided higher and more stable reactivity over 20 cycles in both operating regimes, indicating an optimal balance between the two reactive phases.

The preparation method proved to be a key parameter governing phase interaction and energy storage contribution. Dry ball milling enhanced CaO reactivity under mild conditions but led to accelerated deactivation under severe operation. Freeze granulation promoted $Cu_2O$ activity yet showed lower performance under mild cycling. Wet ball milling yielded a WCa50Cu50 composite exhibiting the most balanced behavior, combining sustained CaO conversion, stable $Cu_2O$ activity, and reduced deactivation over repeated cycles. This composite was consistently identified as having the best overall performance across both operating regimes. Although FCa50Cu50 showed slightly higher accumulated energy storage under severe conditions, its inferior performance under mild conditions resulted in a less favorable overall balance. WCa50Cu50 therefore represents the most robust compromise between efficiency and stability.

Structural, morphological, optical and thermal characterization of WCa50Cu50 supported these findings. XRD analysis revealed the formation of $Ca_2CuO_3$ as an intermediate compound under both operating conditions, but in different relative proportions. SEM-EDX analyses showed segregation of Ca- and Cu-rich domains after cycling, more pronounced under severe conditions. Optical and thermal measurements evidenced significant enhancements in solar absorptance and thermal conductivity, respectively, compared to $CaCO_3$.

Overall, the results demonstrate that $CaCO_3$/CuO composites prepared by wet ball milling emerge as promising candidates for integrated thermochemical energy storage systems, combining high energy density, improved cycling stability, and enhanced optical and thermal properties.

## Author contributions

Mónica Salazar-Lago: investigation, formal analysis. Ana Castro-Chincho: investigation, formal analysis. Pedro E. Sánchez-Jiménez: conceptualization, supervision, resources. Luis A. Pérez-Maqueda: conceptualization, supervision, writing – reviewing and editing, funding acquisition. Antonio Perejón: writing – original draft, writing – reviewing and editing, supervision.

## Conflicts of interest

There are no conflicts of interest to declare.

## Data availability

Data for this article are available at DIGITAL.CSIC at https://doi.org/10.20350/digitalCSIC/18164.

Supplementary information (SI) is available. See DOI: https://doi.org/10.1039/d6ta02200f.

## Acknowledgements

Financial support is acknowledged from grant PID2022-140815OB-C22 funded by MCIN/AEI/10.13039/501100011033 and ERDF – A way of making Europe. Financial support provided by VII PPIT of the University of Seville for the use of the General Research Services (CITIUS) is acknowledged.

## References

1 X. Peng, T. W. Root and C. T. Maravelias, Storing solar energy with chemistry: The role of thermochemical storage in

concentrating solar power, *Green Chem.*, 2017, **19**(10), 2427–2438.
2 M. T. Islam, N. Huda, A. B. Abdullah and R. Saidur, A comprehensive review of state-of-the-art concentrating solar power (CSP) technologies: Current status and research trends, *Renewable Sustainable Energy Rev.*, 2018, **91**, 987–1018.
3 A. G. Fernández, J. Gomez-Vidal, E. Oró, A. Kruizenga, A. Solé and L. F. Cabeza, Mainstreaming commercial CSP systems: A technology review, *Renewable Energy*, 2019, **140**, 152–176.
4 A. Bonk, S. Sau, N. Uranga, M. Hernaiz and T. Bauer, Advanced heat transfer fluids for direct molten salt line-focusing CSP plants, *Prog. Energy Combust. Sci.*, 2018, **67**, 69–87.
5 J. Cot-Gores, A. Castell and L. F. Cabeza, Thermochemical energy storage and conversion: A-state-of-the-art review of the experimental research under practical conditions, *Renewable Sustainable Energy Rev.*, 2012, **16**(7), 5207–5224.
6 A. Solé, X. Fontanet, C. Barreneche, A. I. Fernández, I. Martorell and L. F. Cabeza, Requirements to consider when choosing a thermochemical material for solar energy storage, *Sol. Energy*, 2013, **97**, 398–404.
7 X. Chen, Z. Zhang, C. Qi, X. Ling and H. Peng, State of the art on the high-temperature thermochemical energy storage systems, *Energy Convers. Manage.*, 2018, **177**, 792–815.
8 A. J. Carrillo, J. González-Aguilar, M. Romero and J. M. Coronado, Solar Energy on Demand: A Review on High Temperature Thermochemical Heat Storage Systems and Materials, *Chem. Rev.*, 2019, **119**(7), 4777–4816.
9 A. Bayon, R. Bader, M. Jafarian, L. Fedunik-Hofman, Y. Sun, J. Hinkley, S. Miller and W. Lipiński, Techno-economic assessment of solid–gas thermochemical energy storage systems for solar thermal power applications, *Energy*, 2018, **149**, 473–484.
10 T. D. Humphries, K. T. Møller, W. D. A. Rickard, M. V. Sofianos, S. Liu, C. E. Buckley and M. Paskevicius, Dolomite: A low cost thermochemical energy storage material, *J. Mater. Chem. A*, 2019, **7**(3), 1206–1215.
11 F. Raganati and P. Ammendola, Review of Carbonate-Based Systems for Thermochemical Energy Storage for Concentrating Solar Power Applications: State-of-the-Art and Outlook, *Energy Fuels*, 2023, **37**(3), 1777–1808.
12 R. Chacartegui, A. Alovisio, C. Ortiz, J. M. Valverde, V. Verda and J. A. Becerra, Thermochemical energy storage of concentrated solar power by integration of the calcium looping process and a $CO_2$ power cycle, *Appl. Energy*, 2016, **173**, 589–605.
13 W. G. Le Roux, T. Bello-Ochende and J. P. Meyer, Operating conditions of an open and direct solar thermal Brayton cycle with optimised cavity receiver and recuperator, *Energy*, 2011, **36**(10), 6027–6036.
14 E. Koepf, S. G. Advani, A. Steinfeld and A. K. Prasad, A novel beam-down, gravity-fed, solar thermochemical receiver/reactor for direct solid particle decomposition: Design, modeling, and experimentation, *Int. J. Hydrogen Energy*, 2012, **37**(22), 16871–16887.
15 S. Padula, M. Troiano, C. Tregambi, R. Solimene and P. Salatino, Directly irradiated fluidized bed autothermal reactor (DIFBAR): Hydrodynamics, thermal behaviour and preliminary reactive tests, *Fuel*, 2023, **346**, 128222.
16 C. K. Ho and B. D. Iverson, Review of high-temperature central receiver designs for concentrating solar power, *Renewable Sustainable Energy Rev.*, 2014, **29**, 835–846.
17 J. S. Prasad, P. Muthukumar, F. Desai, D. N. Basu and M. M. Rahman, A critical review of high-temperature reversible thermochemical energy storage systems, *Appl. Energy*, 2019, **254**, 113733.
18 M. T. Dunstan, F. Donat, A. H. Bork, C. P. Grey and C. R. Müller, $CO_2$ Capture at Medium to High Temperature Using Solid Oxide-Based Sorbents: Fundamental Aspects, Mechanistic Insights, and Recent Advances, *Chem. Rev.*, 2021, **121**(20), 12681–12745.
19 B. Sarrión, A. Perejón, P. E. Sánchez-Jiménez, N. Amghar, R. Chacartegui, J. Manuel Valverde and L. A. Pérez-Maqueda, Calcination under low $CO_2$ pressure enhances the calcium Looping performance of limestone for thermochemical energy storage, *Chem. Eng. J.*, 2021, **417**, 127922.
20 C. Tregambi, P. Salatino, R. Solimene and F. Montagnaro, An experimental characterization of Calcium Looping integrated with concentrated solar power, *Chem. Eng. J.*, 2018, **331**, 794–802.
21 C. Ortiz, J. M. Valverde, R. Chacartegui, L. A. Perez-Maqueda and P. Giménez, The Calcium-Looping ($CaCO_3$/CaO) process for thermochemical energy storage in Concentrating Solar Power plants, *Renewable Sustainable Energy Rev.*, 2019, **113**, 109252.
22 R. Chacartegui, G. Gravanis, A. Carro, C. Ortiz, L. A. Pérez-Maqueda, N. Amghar, C. Tejada, G. Karagiannakis, I. N. Tsimpanogiannis, S. Papadopoulou and S. Voutetakis, Carbonation tests in a kW-scale entrained flow reactor for thermochemical energy storage using the calcium looping-based system, *Chem. Eng. J.*, 2025, **524**, 169801.
23 A. A. Scaltsoyiannes and A. A. Lemonidou, On the factors affecting the deactivation of limestone under calcium looping conditions: A new comprehensive model, *Chem. Eng. Sci.*, 2021, **243**, 116797.
24 L. Teng, Y. M. Xuan, Y. Da, X. L. Liu and Y. L. Ding, Modified Ca-Looping materials for directly capturing solar energy and high-temperature storage, *Energy Storage Mater.*, 2020, **25**, 836–845.
25 H. Zhang, C. Xu, B. Xu, X. Sun, J. Xing and Z. Liao, Study on heat transport analysis and improvement method in a single $CaCO_3$ pellet for thermochemical energy storage, *Appl. Therm. Eng.*, 2024, **248**, 123145.
26 D. Rodrigues, C. I. C. Pinheiro, R. M. Filipe, L. F. Mendes and H. A. Matos, Optimization of an improved calcium-looping process for thermochemical energy storage in concentrating solar power plants, *J. Energy Storage*, 2023, **72**, 108199.
27 K. T. Moller, A. Ibrahim, C. E. Buckley and M. Paskevicius, Inexpensive thermochemical energy storage utilising

additive enhanced limestone, *J. Mater. Chem. A*, 2020, **8**(19), 9646–9653.

28 B. Sarrión, A. Perejón, P. E. Sánchez-Jiménez, L. A. Pérez-Maqueda and J. M. Valverde, Role of calcium looping conditions on the performance of natural and synthetic Ca-based materials for energy storage, *J. $CO_2$ Util.*, 2018, **28**, 374–384.

29 C. Tregambi, E. Mancusi, P. Bareschino, F. Pepe, S. Scognamiglio, G. Landi and R. Solimene, Kinetics and Redox Activity of Copper/Cerium Mixed Oxides ($CuO/CeO_2$) for Thermochemical Energy Storage Applications, *Ind. Eng. Chem. Res.*, 2026, **65**(1), 312–325.

30 F. Raganati, R. Chirone and P. Ammendola, Calcium-looping for thermochemical energy storage in concentrating solar power applications: Evaluation of the effect of acoustic perturbation on the fluidized bed carbonation, *Chem. Eng. J.*, 2020, **392**, 123658.

31 F. Y. Chai, P. W. Zhu, H. R. Xu, X. Y. Xie and G. Xiao, Mn and Al co-modified CaO-based composites from various calcium precursors for thermochemical energy storage: High energy storage density and excellent solar absorption ability, *Sol. Energy Mater. Sol. Cells*, 2024, **269**, 112761.

32 S. J. Guo, X. K. Tian, J. Yan, S. H. Ju and C. Y. Zhao, Performance enhancement mechanisms of calcium-based thermochemical energy storage compounds: insights from first-principles and experimental investigations, *J. Mater. Chem. A*, 2024, **12**(23), 14129–14147.

33 Y. Shi, J. Sun, R. Wang, Y. Long, R. Wang, Z. Zhou, S. Wu, X. E. Cao and C. Zhao, Collaborative Design of Light-Absorbing Shell Wrapping and Inner Thermal Conductivity Enhancing for Ca-Based Thermochemical Heat Storage Pellets, *Adv. Funct. Mater.*, 2026, **36**(19), e21241.

34 T. Block and M. Schmücker, Metal oxides for thermochemical energy storage: A comparison of several metal oxide systems, *Sol. Energy*, 2016, **126**, 195–207.

35 B. Bulfin, J. Vieten, C. Agrafiotis, M. Roeb and C. Sattler, Applications and limitations of two step metal oxide thermochemical redox cycles; a review, *J. Mater. Chem. A*, 2017, **5**(36), 18951–18966.

36 S. K. Wu, C. Zhou, E. Doroodchi, R. Nellore and B. Moghtaderi, A review on high-temperature thermochemical energy storage based on metal oxides redox cycle, *Energy Convers. Manage.*, 2018, **168**, 421–453.

37 M. Gigantino, S. Sas Brunser and A. Steinfeld, High-Temperature Thermochemical Heat Storage via the CuO/$Cu_2O$ Redox Cycle: From Material Synthesis to Packed-Bed Reactor Engineering and Cyclic Operation, *Energy Fuels*, 2020, **34**(12), 16772–16782.

38 D. Müller, C. Knoll, W. Artner, M. Harasek, C. Gierl-Mayer, J. M. Welch, A. Werner and P. Weinberger, Combining in-situ X-ray diffraction with thermogravimetry and differential scanning calorimetry – An investigation of $Co_3O_4$, $MnO_2$ and $PbO_2$ for thermochemical energy storage, *Sol. Energy*, 2017, **153**, 11–24.

39 A. J. Carrillo, D. Sastre, D. P. Serrano, P. Pizarro and J. M. Coronado, Revisiting the $BaO_2$/BaO redox cycle for solar thermochemical energy storage, *Phys. Chem. Chem. Phys.*, 2016, **18**(11), 8039–8048.

40 A. J. Carrillo, D. P. Serrano, P. Pizarro and J. M. Coronado, Improving the Thermochemical Energy Storage Performance of the $Mn_2O_3/Mn_3O_4$ Redox Couple by the Incorporation of Iron, *ChemSusChem*, 2015, **8**(11), 1947–1954.

41 C. Pagkoura, G. Karagiannakis, A. Zygogianni, S. Lorentzou, M. Kostoglou, A. G. Konstandopoulos, M. Rattenburry and J. W. Woodhead, Cobalt oxide based structured bodies as redox thermochemical heat storage medium for future CSP plants, *Sol. Energy*, 2014, **108**, 146–163.

42 A. J. Schrader, A. P. Muroyama and P. G. Loutzenhiser, Solar electricity via an Air Brayton cycle with an integrated two-step thermochemical cycle for heat storage based on $Co_3O_4$/CoO redox reactions: Thermodynamic analysis, *Sol. Energy*, 2015, **118**, 485–495.

43 M. Deutsch, F. Horvath, C. Knoll, D. Lager, C. Gierl-Mayer, P. Weinberger and F. Winter, High-Temperature Energy Storage: Kinetic Investigations of the CuO/$Cu_2O$ Reaction Cycle, *Energy Fuels*, 2017, **31**(3), 2324–2334.

44 M. Silakhori, M. Jafarian, M. Arjomandi and G. J. Nathan, Thermogravimetric analysis of Cu, Mn, Co, and Pb oxides for thermochemical energy storage, *J. Energy Storage*, 2019, **23**, 138–147.

45 X. K. Tian, S. C. Lin, J. Yan and C. Y. Zhao, Sintering mechanism of calcium oxide/calcium carbonate during thermochemical heat storage process, *Chem. Eng. J.*, 2022, **428**, 131229.

46 P. Haseli, M. Jafarian and G. J. Nathan, High temperature solar thermochemical process for production of stored energy and oxygen based on CuO/$Cu_2O$ redox reactions, *Sol. Energy*, 2017, **153**, 1–10.

47 M. Rahman, D. Korba, J. Zhao, N. AuYeung and L. Li, Thermochemical energy storage in a lab-scale packed-bed reactor using MgO supported $BaO_2$/BaO redox system, *J. Energy Storage*, 2025, **133**, 117917.

48 J. Ortiz-Ulloa, O. Ramsey, P. Schimmels, M. Hayes, D. Korba, K. Randhir, N. Ozalp, L. Li, J. Petrasch, J. Klausner, A. Benard and N. AuYeung, Conversion of stored thermochemical potential into high quality heat in a continuous flow reactor/heat exchanger, *J. Mater. Chem. A*, 2025, **13**(38), 32481–32503.

49 J. Chen, F. Donat, L. Duan, A. M. Kierzkowska, S. M. Kim, Y. Xu, E. J. Anthony and C. R. Müller, Metal-oxide stabilized CaO/CuO composites for the integrated Ca/Cu looping process, *Chem. Eng. J.*, 2021, **403**, 126330.

50 C. Qin, J. Yin, C. Luo, H. An, W. Liu and B. Feng, Enhancing the performance of CaO/CuO based composite for $CO_2$ capture in a combined Ca–Cu chemical looping process, *Chem. Eng. J.*, 2013, **228**, 75–86.

51 J. Chen, L. Duan, T. Shi, R. Bian, Y. Lu, F. Donat and E. J. Anthony, A facile one-pot synthesis of CaO/CuO hollow microspheres featuring highly porous shells for enhanced $CO_2$ capture in a combined Ca–Cu looping process via a template-free synthesis approach, *J. Mater. Chem. A*, 2019, **7**(37), 21096–21105.

 

52 Y. Zhu, K. Mimura and M. Isshiki, Oxidation Mechanism of $Cu_2O$ to CuO at 600–1050°C, *Oxid. Met.*, 2004, **62**(3), 207–222.
53 M. Benitez-Guerrero, J. M. Valverde, A. Perejon, P. E. Sanchez-Jimenez and L. A. Perez-Maqueda, Effect of milling mechanism on the $CO_2$ capture performance of limestone in the Calcium Looping process, *Chem. Eng. J.*, 2018, **346**, 549–556.
54 P. E. Sánchez-Jiménez, J. M. Valverde, A. Perejón, A. de la Calle, S. Medina and L. A. Pérez-Maqueda, Influence of Ball Milling on CaO Crystal Growth During Limestone and Dolomite Calcination: Effect on $CO_2$ Capture at Calcium Looping Conditions, *Cryst. Growth Des.*, 2016, **16**(12), 7025–7036.
55 J. D. Durán-Martín, P. E. Sánchez Jimenez, J. M. Valverde, A. Perejón, J. Arcenegui-Troya, P. García Triñanes and L. A. Pérez Maqueda, Role of particle size on the multicycle calcium looping activity of limestone for thermochemical energy storage, *J. Adv. Res.*, 2020, **22**, 67–76.
56 A. A. Burdina, O. V. Merkulov, A. A. Markov and M. V. Patrakeev, Evaluation of $Ca_2CuO_3$ as an oxygen carrier material, *Mater. Lett.*, 2021, **297**, 129968.
57 E. Hassani, J. Cho, F. Feyzbar-Khalkhali-Nejad, A. Rashti, S. S. Jang and T.-S. Oh, $Ca_2CuO_3$: A high temperature $CO_2$ sorbent with rapid regeneration kinetics, *J. Environ. Chem. Eng.*, 2022, **10**(2), 107334.
58 E. Hassani, F. Feyzbar-Khalkhali-Nejad, A. Rashti and T.-S. Oh, Solid-state decomposition of $Ca_2CuO_3$ enhances its $CO_2$ reactivity and cycle stability, *Fuel*, 2023, **332**, 126160.
59 V. Moreno, J. Arcenegui-Troya, P. Enrique Sánchez-Jiménez, A. Perejón, R. Chacartegui, J. Manuel Valverde and L. Allan Pérez-Maqueda, Albero: An alternative natural material for solar energy storage by the calcium-looping process, *Chem. Eng. J.*, 2022, **440**, 135707.